*J. Fluid Mech.* (2025), *vol.* 1025, A34, doi:10.1017/jfm.2025.10921

# Slip slender-body theory

**Yi Man**[1], **Lyndon Koens**[2,3] **and Eric Lauga**[4]

[1]School of Mechanics and Engineering Science, State Key Laboratory for Turbulence and Complex Systems, Peking University, Beijing 100871, PR China

[2]Department of Mathematics, University of Hull, Hull HU6 7RX, UK

[3]Discipline of Mathematics, University of Adelaide, Adelaide 5005, Australia

[4]Department of Applied Mathematics and Theoretical Physics, University of Cambridge, Cambridge CB3 0WA, UK

**Corresponding authors:** Yi Man, yiman@pku.edu.cn; Eric Lauga, e.lauga@damtp.cam.ac.uk

(Received 2 April 2025; revised 26 September 2025; accepted 27 October 2025)

Slip effects on solid boundaries are common in complex fluids. Boundary depletion layers in polymer solutions can create apparent slip effects, which can in turn significantly impact the dynamics of moving bodies. Motivated by microswimmer locomotion in such environments, we derive a series of slip slender-body theories for filamentous bodies experiencing slip-like boundary conditions. Using Navier's slip model, we derive three slip slender-body theories, linking the body's velocity to the distribution of hydrodynamic forces. The models are shown to be consistent with each other and with existing numerical computations. As the slip length increases, we show that the drag parallel to the body decreases towards zero while the perpendicular drag remains finite, in a manner which we quantify. This reduction in drag ratio is shown to be inversely related to microswimmer mobility in two simple swimmer models. This increase could help rationalise empirically observed enhanced swimming in complex fluids.

**Key words:** slender-body theory

## 1. Introduction

Slender-body theory (SBT) models the dynamics of elongated bodies, whose lengths are significantly greater than their diameter, in a viscous fluid (Lauga 2020). Derived through a systematic asymptotic expansion, SBT relates the body's velocity to the viscous drag it experiences. It has been instrumental in the study of the microscopic biological world and the motility of microscopic organisms/machines. For example, it has been used to study bacterial swimming (Lauga 2016), the role of microtubules in cell division (Shelley 2016), the propulsion generated from helical filaments (Rodenborn *et al.* 2013; Jawed *et al.* 2015; Riley, Das & Lauga 2018), the undulatory motion of spermatozoa (Gillies *et al.* 2009;

Smith *et al.* 2009), the hydrodynamics of polymers and fibres (Guglielmini *et al.* 2012) and the behaviour of synthetic swimmers (Roper *et al.* 2006).

Historically, several versions of SBT have been developed. Each version asymptotically expands the flow in the aspect ratio of the body (defined as the thickness divided by length) to varying levels of accuracy. The resistive-force theory (RFT) approach expresses the solution as a power series in the logarithm of the aspect ratio, with the logarithm arising from the flow around an infinite cylinder (Batchelor 1970; Cox 1970; Keller & Rubinow 1976). The RFT provides analytical solutions but has low accuracy because logarithmic growth is slow, so models with algebraic (instead of logarithmic) accuracy were developed to overcome this disadvantage. Typically obtained by placing hydrodynamic singularities along the centreline of the body, these SBT versions offer higher accuracy at the cost of being semi-numerical. Lighthill (1976) first developed an algebraic model placing stokeslets (point forces) along the centreline of the body and source dipoles in a local region near the point of interest. Johnson (1980) improved on Lighthill's model using a prolate spheroidal body shape and the known singularity representation for this shape (Chwang & Wu 1975). More recent work has extended these SBTs to include non-circular cross-sections (Koens & Lauga 2016; Borker & Koch 2019), the rotational motion of filaments (Maxian & Donev 2022; Walker, Ishimoto & Gaffney 2023), higher accuracy (Koens 2022) and obstacles (Man, Koens & Lauga 2016; Koens & Montenegro-Johnson 2021; Koens & Walker 2024). Mathematical studies have also further bounded the accuracy of classical SBTs (Childress 1981; Mori & Ohm 2021; Ohm 2024).

Most SBTs have been developed for bodies moving in Newtonian fluids with no-slip boundaries. When the surrounding medium departs from this ideal, the classical no-slip SBT is no longer applicable and alternative models such as the viscoplastic RFT of Hewitt & Balmforth (2018) or the empirical shear-thinning theory of Riley & Lauga (2017) have therefore been proposed. Indeed, biological fluids are often characterised by non-Newtonian rheology. The blood and the mucus in the lung, gut or cervix all display non-Newtonian fluid characteristics (Roselli & Diller 2011). In recent years, many studies have explored how non-Newtonian effects influence the swimming speeds of microorganisms and micromachines, revealing that motion of swimmers in non-Newtonian fluids can change significantly (Li, Lauga & Ardekani 2021; Spagnolie & Underhill 2023). For example, the locomotion of *E. coli* bacteria, theoretical squirmers and Janus particles is enhanced in shear-thinning fluids (Qu & Breuer 2020; van Gogh *et al.* 2022; Zhu *et al.* 2024). This enhancement depends critically on the reduction of viscosity near the swimmer (Gómez *et al.* 2017; Demir *et al.* 2020). Likewise, in polymer solutions the swimming speed of microorganisms increases with polymer concentration (Gagnon, Shen & Arratia 2013; Patteson *et al.* 2015), although the underlying mechanism remains unclear.

The enhancement of swimming in polymer solutions can be rationalised theoretically by the presence of an 'apparent slip' near the body of the microswimmers (Man & Lauga 2015). Apparent slip occurs in polymer solutions when polymer molecules are on average displaced away from a boundary, often due to entropic effects that drive the polymers to regions of higher configurational freedom, creating a depletion region with a lower effective viscosity adjacent to the wall (Cohen & Metzner 1985). Flows over this layer can then display a rapid increase in velocity near the wall. If the region is thin relative to the bulk length scales, this rapid increase appears (if extrapolated linearly) to violate the no-slip boundary condition, leading to an apparent slip (Mhetar & Archer 1998). Apparent slip has classically also been reported in hydrophobic microchannels (Choi, Westin & Breuer 2003), shear-thinning fluids (Patlazhan & Vagner 2017) and rarefied gas problems (Nassios & Sader 2012). Likewise, slip effects have been invoked in nanomaterials, such as graphene and carbon nanotubes (Walther *et al.* 2004), when the liquid is in contact

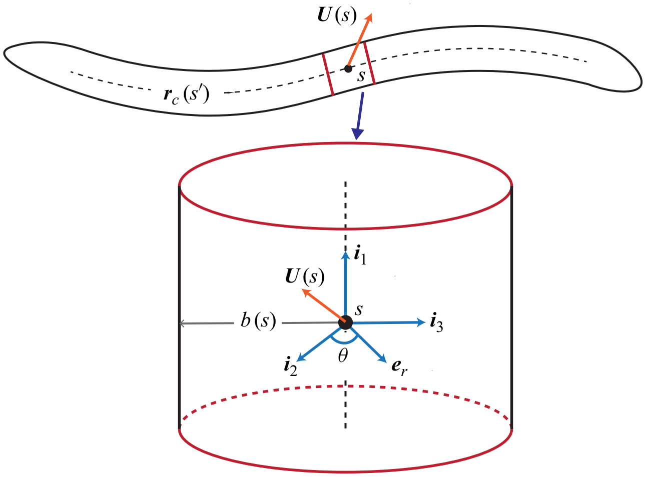

Figure 1. Top: Geometry of slender body, with total length $L$, and local cross-sectional radius $b(s)$ changing along the centreline $\boldsymbol{r}_c(s)$. The centreline moves with instantaneous velocity $\boldsymbol{U}(s)$. Bottom: Two frames are defined in this set-up; $\boldsymbol{e}_r$ denotes the radial unit vector in the local cylindrical coordinate system and $[\boldsymbol{i}_1, \boldsymbol{i}_2, \boldsymbol{i}_3]$ is the local Cartesian coordinate frame. The ratio of the cross-sectional radius to the total length, $b/L$, is a small parameter everywhere.

with atomically smooth surfaces (Tocci, Joly & Michaelides 2014). Recently, Kamal, Gravelle & Botto (2020) observed that rigid nanoplatelets can reach stable orientations in shear flow due to a small amount of slip, instead of the classical Jeffery's orbits for no-slip particles. A version of SBT that incorporates slip would thus provide a systematic approach to explore the altered hydrodynamics within these systems.

In this paper, we rigorously develop SBTs that incorporate the experimentally validated Navier slip boundary conditions, in which the tangential slip velocity is linearly proportional to the wall shear rate (Navier 1823). Inspired by the classical works of Cox (1970), Johnson (1980) and Lighthill (1975), we derive three successive versions of the slip SBT, validate the results against existing numerical results and investigate the influence of slip on the propulsion of two simple swimmers. We find that as the slip length increases, the parallel drag decreases towards zero, while the perpendicular drag converges to a finite value. Consequently, the ratio of parallel to perpendicular drag coefficients decreases as the slip length increases, which serves as a potential mechanism to enhance the mobility of microswimmers in complex fluids.

## 2. Geometry and mathematical set-up

### 2.1. *Set-up*

We consider the motion of a body in a viscous fluid with centreline $\boldsymbol{r}_c(s)$ and circular cross-section of local radius $b(s)$, where $s$ is the arc length parameter varying from 0 to the total length $L$; the body is illustrated in figure 1 (top). The aspect ratio of the body is

$$\epsilon = b_0/L, \tag{2.1}$$

where $b_0$ is the maximum value of $b(s)$. At each point along the centreline $\boldsymbol{r}_c(s)$ we define a local Cartesian frame $[\boldsymbol{i}_1(s), \boldsymbol{i}_2(s), \boldsymbol{i}_3(s)]$, where $\boldsymbol{i}_1(s) = \boldsymbol{t}(s)$ is the unit tangent vector at that point (see figure 1, bottom). The in-plane vectors $\boldsymbol{i}_2$ and $\boldsymbol{i}_3$ are then defined such that the local, instantaneous velocity of the slender body $\boldsymbol{U}(s)$ can always be written as

$$\boldsymbol{U}(s) = U_1\, \boldsymbol{i}_1 + U_2\, \boldsymbol{i}_2. \tag{2.2}$$

Using this local frame, we define the azimuthal angle $\theta$ in the normal plane, and express the radial and angular directions as

$$\boldsymbol{e}_r = \cos\theta\, \boldsymbol{i}_2 + \sin\theta\, \boldsymbol{i}_3, \quad \boldsymbol{e}_\theta = -\sin\theta\, \boldsymbol{i}_2 + \cos\theta\, \boldsymbol{i}_3. \tag{2.3}$$

We describe the surface of the slender body using a local cylindrical coordinate system $[\boldsymbol{i}_1, \boldsymbol{e}_r, \boldsymbol{e}_\theta]$. The position of a point on the surface is then given by

$$\boldsymbol{r}_S = \boldsymbol{r}_c(s) + b(s)\boldsymbol{e}_r(s, \theta). \tag{2.4}$$

The fluid around the body is assumed to satisfy the incompressible Stokes equations

$$\mu\nabla^2\boldsymbol{u} = \boldsymbol{\nabla} p, \quad \boldsymbol{\nabla}\boldsymbol{\cdot}\boldsymbol{u} = 0, \tag{2.5}$$

where $\boldsymbol{u}(\boldsymbol{r})$ is the fluid velocity at position $\boldsymbol{r}$, $\mu$ is the dynamic viscosity of the fluid and $p(\boldsymbol{r})$ is the dynamic pressure. The surface velocity of the slender body, $\boldsymbol{U}(s)$, is assumed to only vary with the arclength of the body, $s$. Navier's classical slip boundary condition (Navier 1823) is applied everywhere on the filament surface; the normal component of the velocity at a surface is thus continuous while the tangential component has a jump that is proportional to the local strain rate. The proportionality coefficient is called the slip length, $\varLambda$, whose value depends empirically on the environment and the surface material. For example, in polymer solutions the apparent slip length takes values in the range $\varLambda = 0.1-10\ \mu\text{m}$ (Mhetar & Archer 1998).

On the surface of the slender body Navier's slip boundary condition can be written formally as

$$\boldsymbol{u}(\boldsymbol{r}_S) = \boldsymbol{U} + 2\varLambda(\boldsymbol{I} - \boldsymbol{e}_r\boldsymbol{e}_r)\boldsymbol{\cdot}\boldsymbol{E}|_{\boldsymbol{r}_S}\boldsymbol{\cdot}\boldsymbol{e}_r, \tag{2.6}$$

where $2\boldsymbol{E} = \boldsymbol{\nabla}\boldsymbol{u} + (\boldsymbol{\nabla}\boldsymbol{u})^T$ is the strain rate tensor in the fluid. Far from the body the fluid is taken to be at rest, requiring

$$\lim_{|\boldsymbol{r}|\to\infty} \boldsymbol{u}(\boldsymbol{r}) = \boldsymbol{0}. \tag{2.7}$$

### 2.2. *Non-dimensionalisation*

We non-dimensionalise the problem by scaling all lengths by the total length of the slender body, $L$. This produces

$$\bar{s} = \frac{s}{L}, \quad \bar{b} = \frac{b}{L}, \quad \bar{\varLambda} = \frac{\varLambda}{L}, \tag{2.8}$$

where $\bar{s} \in [0, 1]$ and $\bar{b} \in [0, \epsilon]$. Similarly, we scale the velocity by a characteristic velocity $U_0$, making the scaled velocity and the pressure

$$\bar{\boldsymbol{U}} = \frac{\boldsymbol{U}}{U_0}, \quad \bar{p} = \frac{L}{\mu U_0} p. \tag{2.9}$$

As the slip effect is local, we assume that $\bar{\varLambda} = O(\epsilon)$, i.e. a slip length of the order of the cross-sectional dimension at most. For notational convenience it therefore becomes useful to define

$$\hat{b} = \frac{\bar{b}}{\epsilon}, \quad \hat{\varLambda} = \frac{\bar{\varLambda}}{\epsilon}, \tag{2.10}$$

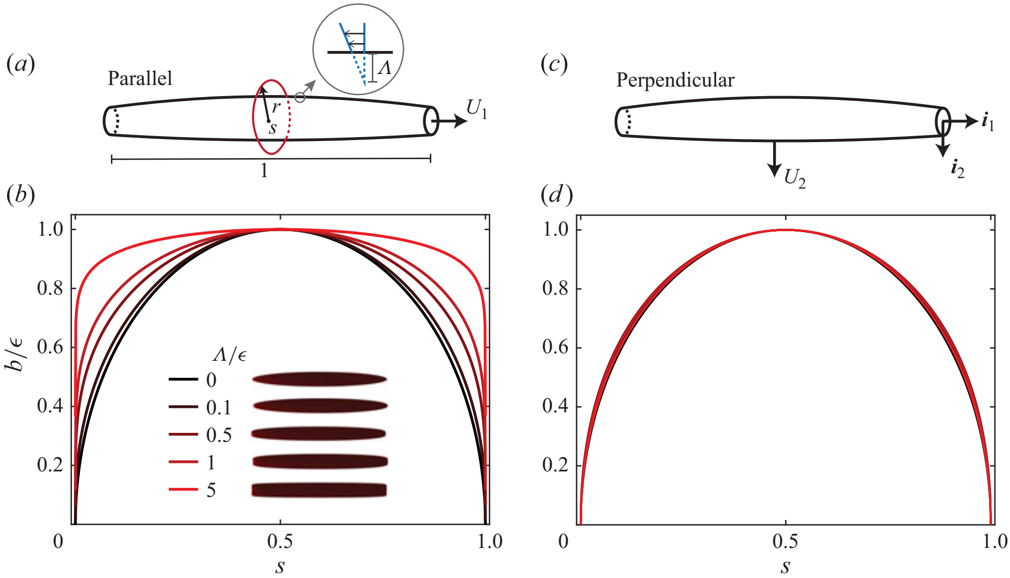

Figure 2. A rigid rod with slip boundary conditions translating parallel to its long axis ($a$,$b$) and perpendicular to it ($c$,$d$). The cross-sectional radii of the rod that generates a constant force per unit length for translation parallel and perpendicular are shown in ($b$,$d$), respectively; the specific shapes displayed in ($a$,$c$) are those with constant force for parallel motion with $\epsilon = 0.05$ and $\Lambda = 1$. Note that the blunt ends are caused by the asymptotic expansion only applying away from the end of the rods and, near the ends, different dependence occurs and so rods may close smoothly.

where $\hat{b} \in [0, 1]$ and $\hat{\Lambda} = O(1)$ are both of order one. This condition on $\hat{\Lambda}$ means that the slip length $\Lambda$ is at most of the order of the body thickness $b$ (but can of course be much smaller than it). Through this scaling the resultant dimensionless equations become

$$\bar{\nabla}^2\bar{\boldsymbol{u}} = \bar{\nabla}\bar{p}, \quad \bar{\nabla}\cdot\bar{\boldsymbol{u}} = 0, \tag{2.11}$$

with boundary conditions

$$\bar{\boldsymbol{u}}(\bar{\boldsymbol{r}}_S) = \bar{\boldsymbol{U}} + 2\bar{\Lambda}(\boldsymbol{I} - \boldsymbol{e}_r\boldsymbol{e}_r)\cdot \bar{\boldsymbol{E}}\big|_{\bar{\boldsymbol{r}}_S}\cdot\boldsymbol{e}_r, \tag{2.12a}$$

$$\bar{\boldsymbol{u}}(\bar{r} \to \infty) = \boldsymbol{0}. \tag{2.12b}$$

We drop all the ‘bars’ in following calculations for simplicity but retain the ‘hats’ for clarity.

## 3. Motion of a straight rigid rod

In this first section, we analyse the motion of a straight rigid rod with slip. We build on the expansions of Hancock (1953) and Lighthill (1975) to determine the leading-order hydrodynamic singularities needed to describe the motion parallel and perpendicular to the axis of the filament. This provides insight into the drag exerted on rods with slip and serves as a foundation for our latter slender-body calculations carried out in § 4.

### 3.1. *Parallel motion*

We first consider a straight slender rod with slip translating along its axis (figure 2$a$,$b$). The rod is aligned with $\boldsymbol{i}_1$, has an arbitrary radius $b(s)$ and translates instantaneously with velocity $\boldsymbol{U} = U_1\boldsymbol{i}_1$. The flow generated from the motion of this rod satisfies (2.11) combined with Navier's slip boundary condition in (2.6). Using the polar coordinates $[\boldsymbol{i}_1, \boldsymbol{e}_r, \boldsymbol{e}_\theta]$, where $r$ denotes the radial distance from the centreline of the rigid rod, the slip condition becomes

$$u_r(r=b)=0, \tag{3.1a}$$

$$u_1(r=b)=U_1+\varLambda\left.\frac{\partial u_1}{\partial r}\right|_{r=b}, \tag{3.1b}$$

where $u_r=\boldsymbol{e}_r\boldsymbol{\cdot}\boldsymbol{u}$ is the radial component of the flow and $u_1=\boldsymbol{i}_1\boldsymbol{\cdot}\boldsymbol{u}$ is its axial component.

We now determine the leading-order hydrodynamic force exerted on the rod using the approaches of Hancock (1953) and Lighthill (1975) except applying the above slip condition instead of the typical no-slip approach. In the asymptotically slender limit, the flow around the rod can be represented as due to a distribution of localised forces of density, $\boldsymbol{f}(s)$, along the centreline of the rod. If this force density is constant, $\boldsymbol{f}=f_1\boldsymbol{i}_1$, the fluid velocity at $\boldsymbol{r}$ is

$$\boldsymbol{u}(\boldsymbol{r})=\frac{f_1}{8\pi}\boldsymbol{i}_1\boldsymbol{\cdot}\int_0^1\left(\frac{\boldsymbol{I}}{R}+\frac{\boldsymbol{R}\boldsymbol{R}}{R^3}\right)\mathrm{d}s', \tag{3.2}$$

where the integrand represents the flow from a point force:

$$\boldsymbol{R}(\boldsymbol{r},s')=\boldsymbol{r}-\boldsymbol{r}_c(s'),\qquad R=|\boldsymbol{R}|. \tag{3.3}$$

To apply the boundary condition we need to evaluate the flow from the above representation near the surface of the rod. For flows near the centreline, the integral in (3.2) can be rewritten as

$$\int_0^1\left(\frac{\boldsymbol{I}}{R}+\frac{\boldsymbol{R}\boldsymbol{R}}{R^3}\right)\mathrm{d}s'=\int_{s-1}^{s}\left[\frac{\boldsymbol{I}}{\sqrt{\varDelta^2+r^2}}+\frac{\varDelta^2\boldsymbol{i}_1\boldsymbol{i}_1+r\Delta(\boldsymbol{i}_1\boldsymbol{e}_r+\boldsymbol{e}_r\boldsymbol{i}_1)+r^2\boldsymbol{e}_r\boldsymbol{e}_r}{(\varDelta^2+r^2)^{3/2}}\right]\mathrm{d}\Delta, \tag{3.4}$$

where $\boldsymbol{r}=\boldsymbol{r}_c(s)+r\boldsymbol{e}_r$, $\boldsymbol{R}=\Delta\boldsymbol{i}_1+r\boldsymbol{e}_r$, $\varDelta=s-s'$ and $r\ll 1$. The largest integrals in this representation are asymptotically given by

$$\int_{s-1}^{s}\frac{1}{\sqrt{\varDelta^2+r^2}}\mathrm{d}\Delta=\ln\frac{4s(1-s)}{r^2}+O\left(r^2\right), \tag{3.5a}$$

$$\int_{s-1}^{s}\frac{\varDelta^2}{(\varDelta^2+r^2)^{3/2}}\mathrm{d}\Delta=\ln\frac{4s(1-s)}{r^2}-2+O\left(r^2\right), \tag{3.5b}$$

$$\int_{s-1}^{s}\frac{r^2}{(\varDelta^2+r^2)^{3/2}}\mathrm{d}\Delta=2+O\left(r^2\right). \tag{3.5c}$$

The remaining integrals are all $O(r)$ or smaller (Koens & Lauga 2018). Hence the integral is approximately

$$\int_0^1\left(\frac{\boldsymbol{I}}{R}+\frac{\boldsymbol{R}\boldsymbol{R}}{R^3}\right)\mathrm{d}s'=\ln\frac{4s(1-s)}{r^2}(\boldsymbol{I}+\boldsymbol{i}_1\boldsymbol{i}_1)-2\boldsymbol{i}_1\boldsymbol{i}_1+2\boldsymbol{e}_r\boldsymbol{e}_r+O\left(r^2\right). \tag{3.6}$$

We note that this expansion is only valid away from the ends of the rod, where $s$ or $1-s$ are of order unity. The fluid velocity near the surface of the rod is therefore

$$\boldsymbol{u}(r)=\frac{f_1}{4\pi}\left[2\ln\frac{2\sqrt{s(1-s)}}{r}-1\right]\boldsymbol{i}_1+O\left(r^2\right). \tag{3.7}$$

Substituting this flow into the boundary conditions, (3.7) into (3.1), reveals that the force must satisfy

$$f_1 = \frac{4\pi U_1}{2\ln\dfrac{2\sqrt{s(1-s)}}{b} - 1 + \dfrac{2\varLambda}{b}} + O\left(\epsilon\right). \tag{3.8}$$

For this force density to be constant the radius $b(s)$ must be chosen such that the right-hand side of (3.8) is constant. If $\varLambda$ is assumed to be constant this implies that

$$\ln\frac{2\sqrt{s(1-s)}}{\hat{b}(s)} + \frac{\hat{\varLambda}}{\hat{b}(s)} = C \quad \forall s, \tag{3.9}$$

where $C$ is a constant and the $\epsilon$ dependence in the logarithm, from (2.10), has been separated out. Assuming that the scaled rod radius, $\hat{b}(s)$, reaches its maximum halfway along the rod, $s = 1/2$, we have $\hat{b}(1/2) = 1$ implying $\hat{\varLambda} = C$. The scaled radius $\hat{b}$ therefore satisfies the transcendental equation

$$\ln\frac{2\sqrt{s(1-s)}}{\hat{b}(s)} + \frac{\hat{\varLambda}}{\hat{b}(s)} = \hat{\varLambda}. \tag{3.10}$$

In figure 2(*b*) we display the constant-force shapes obtained by numerically solving (3.10) for slip lengths of $\hat{\varLambda} = 0,\ 0.1,\ 0.5,\ 1,\ 5$. When there is no slip on the rod ($\hat{\varLambda} = 0$), the rod adopts the classical spheroidal shape. As the slip length increases, the sides of the rod become thicker. This increase is also visible if (3.10) is solved in the small-$\hat{\varLambda}$ limit. Note that this representation of the thickness only applies away from the ends of the rod due to the limitations in the asymptotic expansion. Asymptotically the scaled radius of the body, $\hat{b}$, in this limit is

$$\hat{b}(s) = 2\sqrt{s(1-s)} + \hat{\varLambda}\left(1 - 2\sqrt{s(1-s)}\right) + O\big(\hat{\varLambda}^2\big), \tag{3.11}$$

which always describes a thicker body as $1 - 2\sqrt{s(1-s)} > 0$.

Physically this behaviour reflects the interpretation that the slip length describes an effective penetration depth into the body at which the flow completely stops. Hence if a prolate spheroid without slip has a constant force density, the shape of a body with slip that satisfies the constant force assumption must be thicker than the spheroid in such a way that no slip occurs on an effective spheroid surface.

The results in (3.8) and (3.10) create a linear relationship between the force per unit length on the body and the velocity of the centreline. This suggests that for slender rods we can approximate the force on the rod through a constant drag coefficient, $\xi_1$, of the form

$$f_1 = \xi_1 U_1, \tag{3.12}$$

where

$$\xi_1 = \frac{4\pi}{2\ln\dfrac{2\sqrt{s(1-s)}}{b} - 1 + \dfrac{2\varLambda}{b}} = \frac{2\pi}{\ln\dfrac{2\sqrt{s(1-s)}}{\epsilon\hat{b}} - \dfrac{1}{2} + \dfrac{\hat{\varLambda}}{\hat{b}}} = \frac{2\pi}{\ln\dfrac{1}{\epsilon} - \dfrac{1}{2} + \hat{\varLambda}}. \tag{3.13}$$

### 3.2. *Perpendicular motion*

We now consider the same rod but in the case where it is moving perpendicular to its axis with velocity $\boldsymbol{U} = U_2\boldsymbol{i}_2$ (figure 2*c*,*d*). The slip boundary condition in this case becomes

$$u_r(r=b) = U_2 \cos\theta, \tag{3.14a}$$

$$u_\theta(r=b) = -U_2 \sin\theta + \Lambda \left[ r\frac{\partial}{\partial r}\left(\frac{u_\theta}{r}\right) + \frac{1}{r}\frac{\partial u_r}{\partial \theta}\right]\Bigg|_{r=b}, \tag{3.14b}$$

which again need to be satisfied to solve for the force on the body.

For a constant force density, $\boldsymbol{f}_2 = f_2 \boldsymbol{i}_2$, along the centreline of the body, the resultant flow around the body is

$$\boldsymbol{u}(\boldsymbol{r}) = \frac{f_2}{8\pi}\boldsymbol{i}_2 \boldsymbol{\cdot} \int_0^1 \left(\frac{\boldsymbol{I}}{R} + \frac{\boldsymbol{RR}}{R^3}\right) \mathrm{d}s', \tag{3.15}$$

which, given (3.6), near the rod becomes

$$\boldsymbol{u}(r,\theta) = \frac{f_2}{4\pi}\left[\ln\frac{2\sqrt{s(1-s)}}{r}\,\boldsymbol{i}_2 + \cos\theta\,\boldsymbol{e}_r\right] + O\big(r^2\big). \tag{3.16}$$

Unlike in the parallel case, the flow induced by the force density cannot directly satisfy the slip boundary conditions. This is apparent through the $\boldsymbol{e}_r$ term in the flow. In a classical paper, Lighthill showed source dipoles can be used to remove this $\boldsymbol{e}_r$ contribution (Lighthill 1975). The strengths of these dipoles vary along the centreline and are given by $\boldsymbol{g} = g(s)\boldsymbol{i}_2$. This variation is, however, assumed to be slow allowing for the flow from the dipoles to be approximated by

$$\boldsymbol{u}_d(\boldsymbol{r}) = \frac{g(s)}{4\pi}\boldsymbol{i}_2 \boldsymbol{\cdot} \int_0^1 \left(\frac{\boldsymbol{I}}{R^3} - \frac{3\boldsymbol{RR}}{R^5}\right)\mathrm{d}s' + o(\epsilon), \tag{3.17}$$

where $g(s)$ is the is the dipole strength nearest to the region of interest. Near the surface of the rod the above integral asymptotically evaluates to

$$\int_0^1 \left(\frac{\boldsymbol{I}}{R^3} - \frac{3\boldsymbol{RR}}{R^5}\right)\mathrm{d}s' = \frac{2}{r^2}\left(\boldsymbol{I} - \boldsymbol{i}_1\boldsymbol{i}_1 - 2\boldsymbol{e}_r\boldsymbol{e}_r\right) + O\big(r^2\big). \tag{3.18}$$

Substituting (3.18) into (3.17), the flow induced by the source dipoles can be approximated by

$$\boldsymbol{u}_d(s,r,\theta) = \frac{g}{2\pi r^2}\left[\boldsymbol{i}_2 - 2\cos\theta\boldsymbol{e}_r\right] + O\big(r^2\big). \tag{3.19}$$

The total flow near the surface rod, found by combining (3.16) and (3.19), is

$$\boldsymbol{u}(r,\theta) = \frac{f_2}{4\pi}\left[\ln\frac{2\sqrt{s(1-s)}}{r}\boldsymbol{i}_2 + \cos\theta\boldsymbol{e}_r\right] + \frac{g}{2\pi r^2}\left[\boldsymbol{i}_2 - 2\cos\theta\boldsymbol{e}_r\right] + O\big(r^2\big). \tag{3.20}$$

Substituting (3.20) into the boundary condition (3.14), the slip boundary conditions become

$$f_2\left(\ln\frac{2\sqrt{s(1-s)}}{b} + 1\right) - \frac{2g}{b^2} = 4\pi U_2 + O\big(\epsilon^2\big), \tag{3.21a}$$

$$f_2 \ln\frac{2\sqrt{s(1-s)}}{b} + \frac{2g}{b^2} = 4\pi U_2 - \frac{8\Lambda g}{b^3} + O\left(\epsilon\right). \tag{3.21b}$$

These equations can be solved at leading order in $\epsilon$ for the force and dipole strengths to find

$$g = \frac{b^3}{4(b+2\Lambda)} f_2 + O\left(\epsilon^3\right), \tag{3.22}$$

$$f_2 = \frac{4\pi U_2}{\ln \dfrac{2\sqrt{s(1-s)}}{b} + \dfrac{1}{2} + \dfrac{\Lambda}{b+2\Lambda}} + O(\epsilon). \tag{3.23}$$

Again, $f_2$ is only constant for a certain rod radius $b(s)$. Following the same steps as in the axial translation problem, the radius in the perpendicular translation problem satisfies

$$\ln \frac{2\sqrt{s(1-s)}}{\hat{b}} + \frac{\hat{\Lambda}}{\hat{b}+2\hat{\Lambda}} = \frac{\hat{\Lambda}}{1+2\hat{\Lambda}}. \tag{3.24}$$

We plot in figure 2($d$) the resulting radius, $\hat{b}$, from (3.24) for slip lengths of $\hat{\Lambda} = 0,\ 0.1,\ 0.5,\ 1,\ 5$. When there is no slip on the rod ($\hat{\Lambda} = 0$), the shape is a spheroid. As the slip length increases, the rod appears thicker. However, these changes are less pronounced than the parallel case. This is because the slip factor in the transcendental equation in the parallel case, (3.10), diverges as $\hat{b} \to 0$, while in (3.24) it remains finite for all $\hat{b} \in [0, 1]$. Again we note that this representation of the thickness only applies away from the ends of the rod due to the limitations in the asymptotic expansion.

Here also, (3.23) and (3.24) again create a linear relationship between the force per unit length along the rod and the velocity of the centreline. Hence, this suggests that the force on the rod can be determined through a perpendicular drag coefficient, $\xi_2$, such that

$$f_2 = \xi_2 U_2, \tag{3.25}$$

where

$$\begin{aligned} \xi_2 = \frac{4\pi}{\ln \dfrac{2\sqrt{s(1-s)}}{b} + \dfrac{1}{2} + \dfrac{\Lambda}{b+2\Lambda}} &= \frac{4\pi U_2}{\ln \dfrac{2\sqrt{s(1-s)}}{\epsilon\hat{b}} + \dfrac{1}{2} + \dfrac{\hat{\Lambda}}{\hat{b}+2\hat{\Lambda}}} \\ &= \frac{4\pi}{\ln \dfrac{1}{\epsilon} + \dfrac{1}{2} + \dfrac{\hat{\Lambda}}{1+2\hat{\Lambda}}}. \end{aligned} \tag{3.26}$$

## 4. Slender-body theories

In this section, we now consider the general slender-body problem, defined in § 2, by extending three classical SBTs to incorporate slip. Firstly, following the approach of Cox (1970), we derive the slip RFT, which expresses the force on the body through a logarithmic expansion. Secondly, we use a matched asymptotic expansion, similar to Keller & Rubinow (1976) and Johnson (1980), to derive a similar slip SBT formulation. Finally, we extend the approach from Lighthill (1976), thereby revealing properties of how the inner region scales with the introduction of slip. Unlike the logarithmic expansion resulting from the Cox (1970) approach, the Johnson and Lighthill SBTs are algebraic expansions, providing improved mathematical accuracy at the cost of requiring in general computational evaluation.

### 4.1. *Asymptotic expansion in logarithms: slip resistive-force theory*

The first expansion we consider is a series expansion in logarithms, following the classical approach outlined in Cox (1970). Though less accurate than algebraic models derived later, this approach is fully analytical and, historically, was one of the earliest formulations of SBT. As with all the approaches, this methods considers the behaviour of the slender body in an inner region, in which the body looks like an infinite cylinder, and matches it with an outer region, in which the body acts on the fluid as an infinitesimal line.

#### 4.1.1. *Inner solution*

A regular perturbation expansion of the equations for the flow around a slender body, (2.11) and (2.12), in the limit of small aspect ratio, $\epsilon \ll 1$, suggests that the flow around the body closely resembles the flow around an infinite cylinder (Cox 1970). This may appear to be problematic because of the Stokes paradox, which states that no solution exists for the flow around an infinite cylinder which simultaneously satisfies the boundary conditions on the surface and at infinity at zero Reynolds number (due to a logarithmic divergence). The flow around a slender body therefore needs to capture this logarithmic behaviour in an inner region and match it with the behaviour far from the body to overcome this paradox.

The variation along the axis $\boldsymbol{i}_1$ is assumed to be much slower than variation in the plane, $\partial u_1/\partial x_1 \ll \partial u_r/\partial r$ $(r \sim O(\epsilon))$, thereby making the problem quasi-two-dimensional. Hence near $s$, the inner solution approximates the flow around an infinite cylinder with the boundary conditions

$$\boldsymbol{u}(r = b, \theta) = \boldsymbol{U} + 2\varLambda\,[\boldsymbol{I} - \boldsymbol{e}_r\boldsymbol{e}_r] \boldsymbol{\cdot} \boldsymbol{E} \boldsymbol{\cdot} \boldsymbol{e}_r|_{r=b}, \tag{4.1}$$

where $r$ denotes the radial position. Similar to the rod case, we treat each of these velocity components separately initially before combining them at the end of the inner expansion.

For motion perpendicular to $\boldsymbol{i}_1$ $(U_1 = 0)$, the in-plane flow may be found using a streamfunction, $\psi$, defined as

$$u_r = \frac{1}{r}\frac{\partial \psi}{\partial \theta}, \quad u_\theta = -\frac{\partial \psi}{\partial r}. \tag{4.2}$$

This definition automatically satisfies the mass conservation equation $\boldsymbol{\nabla} \boldsymbol{\cdot} \boldsymbol{u} = 0$. The curl of the Stokes equation ($\boldsymbol{\nabla} \times \nabla^2 \boldsymbol{u} = 0$) also shows that $\psi$ satisfies

$$\nabla^4 \psi = 0. \tag{4.3}$$

The general solution to the above equation can be obtained using separation of variables. Retaining the $\cos\theta$ and $\sin\theta$ terms, this general solution becomes

$$\psi(r, \theta) = \left(Ar \ln r + Br + Cr^{-1}\right)\sin\theta + \left(\alpha r \ln r + \beta r + \gamma r^{-1}\right)\cos\theta, \tag{4.4}$$

where $A$, $B$, $C$, $\alpha$, $\beta$ and $\gamma$ are coefficients to be determined by the boundary conditions. The flow around the cylinder therefore is

$$u_r(r, \theta) = \left(A \ln r + B + Cr^{-2}\right)\cos\theta - \left(\alpha \ln r + \beta + \gamma r^{-2}\right)\sin\theta, \tag{4.5a}$$

$$u_\theta(r, \theta) = -\left[A(\ln r + 1) + B - Cr^{-2}\right]\sin\theta - \left[\alpha(\ln r + 1) + \beta - \gamma r^{-2}\right]\cos\theta. \tag{4.5b}$$

The unknown constants in the above need to be determined by substituting the flow solutions into the slip boundary condition, (4.1). In scalar form these boundary conditions can be written as

$$u_r(b,\theta) = U_2\cos\theta, \tag{4.6a}$$

$$u_\theta(b,\theta) = -U_2\sin\theta + \varLambda\left[r\frac{\partial}{\partial r}\left(\frac{u_\theta}{r}\right) + \frac{1}{r}\frac{\partial u_r}{\partial \theta}\right]_{r=b}, \tag{4.6b}$$

providing the linear relationships

$$A\ln b + B + Cb^{-2} = U_2, \tag{4.7a}$$

$$\alpha\ln b + \beta + \gamma b^{-2} = 0, \tag{4.7b}$$

$$A(\ln b + 1) + B - Cb^{-2} = U_2 + 4\varLambda C b^{-3}, \tag{4.7c}$$

$$\alpha(\ln b + 1) + \beta - \gamma b^{-2} = 4\varLambda\gamma b^{-3}. \tag{4.7d}$$

These equations can be solved for $B$, $C$, $\beta$ and $\gamma$ to find

$$B = U_2 - (\ln b + \chi)A, \quad C = b^2\chi A, \quad \beta = -(\ln b + \chi)\alpha, \quad \gamma = b^2\chi\alpha, \tag{4.8}$$

where $\chi = b/2(b + 2\varLambda)$. Hence, the flow field, at $s$, around a cylinder moving perpendicular to its axis becomes

$$\begin{aligned} u_r(r,\theta) = {} & A\left[\ln\frac{r}{b} - \chi + \frac{b^2}{r^2}\chi\right]\cos\theta \\ & - \alpha\left[\ln\frac{r}{b} - \chi + \frac{b^2}{r^2}\chi\right]\sin\theta + U_2\cos\theta, \end{aligned} \tag{4.9a}$$

$$\begin{aligned} u_\theta(r,\theta) = {} & -A\left[\ln\frac{r}{b} + 1 - \chi - \frac{b^2}{r^2}\chi\right]\sin\theta \\ & - \alpha\left[\ln\frac{r}{b} + 1 - \chi - \frac{b^2}{r^2}\chi\right]\cos\theta - U_2\sin\theta. \end{aligned} \tag{4.9b}$$

The remaining unknowns, $A$ and $\alpha$, are to be solved through matching to the outer solution.

For motion along $\boldsymbol{i}_1$ ($U_2 = 0$), the equations to solve simplify further. Because the variation in $z$ is assumed to be negligible, the flow in the axial direction, $u_1$, is decoupled from all other velocity components and $u_1$ therefore satisfies Laplace's equation:

$$\nabla^2 u_1 = 0, \tag{4.10}$$

with the slip boundary condition

$$u_1(b,\theta) = U_1 + \varLambda\left.\frac{\partial u_1}{\partial r}\right|_{r=b}. \tag{4.11}$$

Laplace's equation has the solution

$$u_1 = D\ln r + E, \tag{4.12}$$

where $D$ and $E$ are coefficients corresponding to the axial flow field. When (4.12) is substituted into (4.11) we find

$$u_1(r,\theta) = D\left(\ln\frac{r}{b} + \frac{\varLambda}{b}\right) + U_1, \tag{4.13}$$

where $E = U_1 + D(\varLambda/b - \ln b)$.

The full flow in the inner region is found by adding (4.9) and (4.13) together. Each of these flows contains a $\ln\epsilon$ term, as $b = \epsilon\hat{b}$. For the flow to remain finite as $\epsilon \to 0$, this suggests that the coefficients $A$, $\alpha$ and $D$ must be of the order of $1/\ln\epsilon$. Consequently, we expand these coefficients and flow as (Cox 1970)

$$A = \frac{A^{(1)}}{\ln\epsilon} + \frac{A^{(2)}}{\ln^2\epsilon} + \cdots, \tag{4.14a}$$

$$\alpha = \frac{\alpha^{(1)}}{\ln\epsilon} + \frac{\alpha^{(2)}}{\ln^2\epsilon} + \cdots, \tag{4.14b}$$

$$D = \frac{D^{(1)}}{\ln\epsilon} + \frac{D^{(2)}}{\ln^2\epsilon} + \cdots \tag{4.14c}$$

and

$$\boldsymbol{u} = \boldsymbol{u}^{(0)} + \frac{\boldsymbol{u}^{(1)}}{\ln\epsilon} + \frac{\boldsymbol{u}^{(2)}}{\ln^2\epsilon} + \cdots. \tag{4.15}$$

Hence, at leading order the flow becomes

$$u_r^{(0)} = -[A^{(1)} - U_2]\cos\theta + \alpha^{(1)}\sin\theta, \tag{4.16a}$$

$$u_\theta^{(0)} = [A^{(1)} - U_2]\sin\theta + \alpha^{(1)}\cos\theta, \tag{4.16b}$$

$$u_1^{(0)} = -D^{(1)} + U_1, \tag{4.16c}$$

while at $O(1/\ln\epsilon)$, $\boldsymbol{u}^{(1)}$ is

$$u_r^{(1)} = \left[A^{(1)}\left(\ln\frac{r}{\hat{b}} - \chi\right) - A^{(2)}\right]\cos\theta - \left[\alpha^{(1)}\left(\ln\frac{r}{\hat{b}} - \chi\right) - \alpha^{(2)}\right]\sin\theta, \tag{4.17a}$$

$$\begin{aligned} u_\theta^{(1)} = &- \left[A^{(1)}\left(\ln\frac{r}{\hat{b}} + 1 - \chi\right) - A^{(2)}\right]\sin\theta \\ &- \left[\alpha^{(1)}\left(\ln\frac{r}{\hat{b}} + 1 - \chi\right) - \alpha^{(2)}\right]\cos\theta, \end{aligned} \tag{4.17b}$$

$$u_1^{(1)} = D^{(1)}\left(\ln\frac{r}{\hat{b}} + \frac{\hat{\Lambda}}{\hat{b}}\right) - D^{(2)}, \tag{4.17c}$$

and $\boldsymbol{u}^{(2)}$ at $O(1/\ln^2\epsilon)$ is

$$u_r^{(2)} = \left[A^{(2)}\left(\ln\frac{r}{\hat{b}} - \chi\right) - A^{(3)}\right]\cos\theta - \left[\alpha^{(2)}\left(\ln\frac{r}{\hat{b}} - \chi\right) - \alpha^{(3)}\right]\sin\theta, \tag{4.18a}$$

$$\begin{aligned} u_\theta^{(2)} = &- \left[A^{(2)}\left(\ln\frac{r}{\hat{b}} + 1 - \chi\right) - A^{(3)}\right]\sin\theta \\ &- \left[\alpha^{(2)}\left(\ln\frac{r}{\hat{b}} + 1 - \chi\right) - \alpha^{(3)}\right]\cos\theta, \end{aligned} \tag{4.18b}$$

$$u_1^{(2)} = D^{(2)}\left(\ln\frac{r}{\hat{b}} + \frac{\hat{\Lambda}}{\hat{b}}\right) - D^{(3)}. \tag{4.18c}$$

The above expanded solutions can now be compared with the outer-region solutions to identify the remaining unknown coefficients $A$, $\alpha$, $D$.

### 4.1.2. *Outer solution and matching*

In the outer region the flow scales with the fibre length, $L$, and so the slender body acts on the fluid as an infinitesimal line. Classically, the flow in this region is represented through a force density, $\boldsymbol{f}(s)$, placed on the filament centreline, $\boldsymbol{r}_c(s)$. The fluid velocity at $\boldsymbol{r}$ is therefore

$$\boldsymbol{u}(\boldsymbol{r}) = \frac{1}{8\pi}\int_0^1 \boldsymbol{f}\left(s'\right)\boldsymbol{\cdot}\left(\frac{\boldsymbol{I}}{R} + \frac{\boldsymbol{RR}}{R^3}\right)\mathrm{d}s', \tag{4.19}$$

where

$$\boldsymbol{R}\left(\boldsymbol{r}, s'\right) = \boldsymbol{r} - \boldsymbol{r}_c\left(s'\right), \quad R = |\boldsymbol{R}|. \tag{4.20}$$

This flow and force density must vanish if the filament vanishes (i.e. $\epsilon \to 0$). Since the inner solution was expanded in $1/\ln\epsilon$, the vanishing criteria suggest that the force should be expanded as

$$\boldsymbol{f} = \frac{\boldsymbol{f}^{(1)}}{\ln\epsilon} + \frac{\boldsymbol{f}^{(2)}}{\ln^2\epsilon} + \cdots . \tag{4.21}$$

As a result, the expanded flow becomes

$$\boldsymbol{u}^{(0)} = \boldsymbol{0} \tag{4.22}$$

and

$$\boldsymbol{u}^{(1)} = \frac{1}{8\pi}\int_0^1 \boldsymbol{f}^{(1)}\left(s'\right)\boldsymbol{\cdot}\left(\frac{\boldsymbol{I}}{R} + \frac{\boldsymbol{RR}}{R^3}\right)\mathrm{d}s', \tag{4.23}$$

where the flow orders are the same orders as those listed in the inner solution, (4.15). Comparing the leading-order terms, (4.22) and (4.16), we find

$$A^{(1)} = U_2, \quad \alpha^{(1)} = 0, \quad D^{(1)} = U_1. \tag{4.24}$$

At first order, we need to compare (4.23) around $\boldsymbol{r} \sim \boldsymbol{r}_c$ and (4.17). This requires transforming (4.23) into a form which captures the $\ln r$ dependence in (4.17). This can be achieved by splitting the integral into a local interval, from $s-\delta$ to $s+\delta$, and a non-local part defined as

$$\boldsymbol{u}^{(1)} = \boldsymbol{u}_L^{(1)} + \boldsymbol{u}_{NL}^{(1)}, \tag{4.25}$$

$$\boldsymbol{u}_L^{(1)} = \frac{1}{8\pi}\int_{s-\delta}^{s+\delta} \boldsymbol{f}^{(1)}\left(s'\right)\boldsymbol{\cdot}\left(\frac{\boldsymbol{I}}{R} + \frac{\boldsymbol{RR}}{R^3}\right)\mathrm{d}s', \tag{4.26}$$

$$\boldsymbol{u}_{NL}^{(1)} = \frac{1}{8\pi}\left(\int_0^{s-\delta} + \int_{s+\delta}^1\right)\boldsymbol{f}^{(1)}\left(s'\right)\boldsymbol{\cdot}\left(\frac{\boldsymbol{I}}{R} + \frac{\boldsymbol{RR}}{R^3}\right)\mathrm{d}s', \tag{4.27}$$

where $\boldsymbol{u}_L^{(1)}$ is the local contribution which will generate the $\ln r$ behaviour and $\boldsymbol{u}_{NL}^{(1)}$ is the remaining behaviour. If $\delta$ is small we can further simplify the local term by Taylor-expanding $\boldsymbol{f}^{(1)}(s')$ in the kernel around $s' = s$. This allows the force to be taken outside of the integral, and simplifying the integral in the local term to

$$\boldsymbol{J}(\boldsymbol{r}) = \int_{s-\delta}^{s+\delta}\left(\frac{\boldsymbol{I}}{R} + \frac{\boldsymbol{RR}}{R^3}\right)\mathrm{d}s'. \tag{4.28}$$

Near $\boldsymbol{r}_c(s)$, the position vector can be represented in local cylindrical coordinates defined as $\boldsymbol{r} = \boldsymbol{r}_c(s) + r\boldsymbol{e}_r(s)$, where $\boldsymbol{t}(s) = \partial\boldsymbol{r}_c(s)/\partial s$ is the tangent to the centreline and $\boldsymbol{e}_r(s)$

is the radial director perpendicular to the tangent. Hence (4.20) becomes $\boldsymbol{R}(\boldsymbol{r}, s') = \boldsymbol{r}_c(s) - \boldsymbol{r}_c(s') + r\boldsymbol{e}_r(s)$. In the limit $\delta \to 0$, $\boldsymbol{r}_c(s) - \boldsymbol{r}_c(s')$ can be further simplified to $\Delta \boldsymbol{t}(s)$, making

$$\boldsymbol{R} \approx \boldsymbol{R}_L = \Delta \boldsymbol{t} + r\boldsymbol{e}_r, \quad R \approx R_L = \sqrt{\varDelta^2 + r^2}, \tag{4.29}$$

and (4.28) as

$$\boldsymbol{J} = \int_{-\delta}^{\delta} \left[ \frac{\boldsymbol{I}}{\sqrt{\varDelta^2 + r^2}} + \frac{\Delta^2 \boldsymbol{tt} + r\Delta(\boldsymbol{te}_r + \boldsymbol{e}_r\boldsymbol{t}) + r^2 \boldsymbol{e}_r\boldsymbol{e}_r}{(\varDelta^2 + r^2)^{3/2}} \right] \mathrm{d}\Delta, \tag{4.30}$$

where $\varDelta = s - s'$. These integrals are all similar to those in (3.5) and can be evaluated to

$$\boldsymbol{J} = 2 \ln \frac{2\delta}{r} (\boldsymbol{I} + \boldsymbol{tt}) - 2\boldsymbol{tt} + 2\boldsymbol{e}_r\boldsymbol{e}_r + O\left(\frac{r^2}{\delta^2}\right). \tag{4.31}$$

Similarly, in this limit the non-local integration can be simplified using $\boldsymbol{R} \approx \boldsymbol{R}_0 = \boldsymbol{r}_c(s) - \boldsymbol{r}_c(s')$, $R \approx R_0 = |\boldsymbol{r}_c(s) - \boldsymbol{r}_c(s')|$ to write it as $\boldsymbol{u}_{NL}^{(1)}$:

$$\boldsymbol{u}_{NL}^{(1)} = \frac{1}{8\pi} \left( \int_0^{s-\delta} + \int_{s+\delta}^{1} \right) \boldsymbol{f}^{(1)}(s') \boldsymbol{\cdot} \left( \frac{\boldsymbol{I}}{R_0} + \frac{\boldsymbol{R}_0\boldsymbol{R}_0}{R_0^3} \right) \mathrm{d}s'. \tag{4.32}$$

We note that the non-local integral is finite as the singularity in the kernel has been removed by the local component. These estimates allow us to approximate the outer solution, $\boldsymbol{u}^{(1)}$ near $\boldsymbol{r}_c(s)$, as

$$\boldsymbol{u}^{(1)} = \frac{1}{8\pi} \boldsymbol{f}^{(1)} \boldsymbol{\cdot} \boldsymbol{J} + \boldsymbol{u}_{NL}^{(1)}, \tag{4.33}$$

or in component form

$$\begin{aligned} u_r^{(1)} &= \left[ \frac{f_2^{(1)}}{4\pi} \left( \ln \frac{2\delta}{r} + 1 \right) + \boldsymbol{u}_{NL}^{(1)} \boldsymbol{\cdot} \boldsymbol{i}_2 \right] \cos\theta \\ &\quad + \left[ \frac{f_3^{(1)}}{4\pi} \left( \ln \frac{2\delta}{r} + 1 \right) + \boldsymbol{u}_{NL}^{(1)} \boldsymbol{\cdot} \boldsymbol{i}_3 \right] \sin\theta, \end{aligned} \tag{4.34a}$$

$$\begin{aligned} u_\theta^{(1)} &= \left[ -\frac{f_2^{(1)}}{4\pi} \left( \ln \frac{2\delta}{r} \right) - \boldsymbol{u}_{NL}^{(1)} \boldsymbol{\cdot} \boldsymbol{i}_2 \right] \sin\theta \\ &\quad + \left[ \frac{f_3^{(1)}}{4\pi} \left( \ln \frac{2\delta}{r} \right) + \boldsymbol{u}_{NL}^{(1)} \boldsymbol{\cdot} \boldsymbol{i}_3 \right] \cos\theta, \end{aligned} \tag{4.34b}$$

$$u_1^{(1)} = \frac{f_1^{(1)}}{4\pi} \left( 2 \ln \frac{2\delta}{r} - 1 \right) + \boldsymbol{u}_{NL}^{(1)} \boldsymbol{\cdot} \boldsymbol{i}_1, \tag{4.34c}$$

where $\boldsymbol{f}^{(1)} = f_1^{(1)}\boldsymbol{i}_1 + f_2^{(1)}\boldsymbol{i}_2 + f_3^{(1)}\boldsymbol{i}_3$. Similarly, the first-order terms from the inner solution are

$$u_r^{(1)} = \left[U_2 \ln r - U_2\left(\ln \hat{b} + \chi\right) - A^{(2)}\right]\cos\theta + \alpha^{(2)}\sin\theta, \tag{4.35a}$$

$$u_\theta^{(1)} = -\left[U_2 \ln r - U_2\left(\ln \hat{b} - 1 + \chi\right) - A^{(2)}\right]\sin\theta + \alpha^{(2)}\cos\theta, \tag{4.35b}$$

$$u_1^{(1)} = U_1 \ln r + U_1\left(-\ln \hat{b} + \frac{\hat{\varLambda}}{\hat{b}}\right) - D^{(2)}, \tag{4.35c}$$

where we combined (4.24) and (4.17). The $\ln r$ dependence in (4.34) and (4.35) can be matched to show that the force satisfies

$$f_1^{(1)} = -2\pi U_1, \quad f_2^{(1)} = -4\pi U_2, \quad f_3^{(1)} = 0, \tag{4.36}$$

and the remaining unknown constants must be

$$A^{(2)} = \left(\ln\frac{2\delta}{\hat{b}} + 1 - \chi\right)U_2 - \boldsymbol{u}_{NL}^{(1)}\boldsymbol{\cdot}\boldsymbol{i}_2, \tag{4.37a}$$

$$\alpha^{(2)} = \boldsymbol{u}_{NL}^{(1)}\boldsymbol{\cdot}\boldsymbol{i}_3, \tag{4.37b}$$

$$D^{(2)} = \left(\ln\frac{2\delta}{\hat{b}} + \frac{\hat{\varLambda}}{\hat{b}} - \frac{1}{2}\right)U_1 - \boldsymbol{u}_{NL}^{(1)}\boldsymbol{\cdot}\boldsymbol{i}_1. \tag{4.37c}$$

The second-order correction to the flow can be found using the same procedure. As we are interested in the force per unit length, $\boldsymbol{f}^{(2)}(s)$, we only summarise the major steps to obtain it here. The remaining unknown constants are only needed if solving for the force to the next order. The flow generated by the second-order correction is

$$\boldsymbol{u}^{(2)}(\boldsymbol{r}) = \frac{1}{8\pi}\int_0^1 \boldsymbol{f}^{(2)}(s')\boldsymbol{\cdot}\left(\frac{\boldsymbol{I}}{R} + \frac{\boldsymbol{R}\boldsymbol{R}}{R^3}\right)\mathrm{d}s', \tag{4.38}$$

which, when expanded in the limit $\boldsymbol{r}$ close to $\boldsymbol{r}_c(s)$, is approximately

$$\boldsymbol{u}^{(2)}(\boldsymbol{r}) \sim -\frac{\ln r}{4\pi}\boldsymbol{f}^{(2)}\boldsymbol{\cdot}(\boldsymbol{I} + \boldsymbol{t}\boldsymbol{t}), \tag{4.39}$$

or

$$u_r^{(2)} \sim -\frac{f_2^{(2)}}{4\pi}\ln r\cos\theta - \frac{f_3^{(2)}}{4\pi}\ln r\sin\theta, \tag{4.40a}$$

$$u_\theta^{(2)} \sim \frac{f_2^{(2)}}{4\pi}\ln r\sin\theta - \frac{f_3^{(2)}}{4\pi}\ln r\cos\theta, \tag{4.40b}$$

$$u_1^{(2)} \sim -\frac{f_1^{(2)}}{2\pi}\ln r, \tag{4.40c}$$

where $\boldsymbol{f}^{(2)}$ as $f_1^{(2)}\boldsymbol{i}_1 + f_2^{(2)}\boldsymbol{i}_2 + f_3^{(2)}\boldsymbol{i}_3$. The corresponding inner solution, (4.18), behaves like

$$u_r^{(2)} \sim A^{(2)}\ln r\cos\theta - \alpha^{(2)}\ln r\sin\theta, \tag{4.41a}$$

$$u_\theta^{(2)} \sim -A^{(2)}\ln r\sin\theta - \alpha^{(2)}\ln r\cos\theta, \tag{4.41b}$$

$$u_1^{(2)} \sim D^{(2)}\ln r, \tag{4.41c}$$

showing that the second-order force density satisfies

$$f_1^{(2)} = -2\pi D^{(2)}, \quad f_2^{(2)} = -4\pi A^{(2)}, \quad f_3^{(2)} = 4\pi \alpha^{(2)}. \tag{4.42}$$

### 4.1.3. *Final solution: a compact representation*

The matched solutions, (4.36) and (4.42), for the force can be represented compactly in vector form as

$$\frac{\boldsymbol{f}^{(1)}(s)}{2\pi} = -\boldsymbol{U}(s)\boldsymbol{\cdot}[2\boldsymbol{I} - \boldsymbol{t}(s)\boldsymbol{t}(s)], \tag{4.43a}$$

$$\begin{aligned}\frac{\boldsymbol{f}^{(2)}(s)}{2\pi} &= \left[-\ln\frac{2\delta}{\hat{b}}\boldsymbol{U}(s) + \boldsymbol{u}_{NL}^{(1)}(s)\right]\boldsymbol{\cdot}[2\boldsymbol{I} - \boldsymbol{t}(s)\boldsymbol{t}(s)] \\ &\quad - \boldsymbol{U}(s)\boldsymbol{\cdot}\left\{\left[1 + \frac{2\Lambda}{b+2\Lambda}\right]\boldsymbol{I} + \left[-\frac{3}{2} - \frac{2\Lambda}{b+2\Lambda} + \frac{\Lambda}{b}\right]\boldsymbol{t}(s)\boldsymbol{t}(s)\right\},\end{aligned} \tag{4.43b}$$

where

$$\boldsymbol{u}_{NL}^{(1)}(s) = -\frac{1}{4}\left(\int_0^{s-\delta} + \int_{s+\delta}^1\right)\left\{\boldsymbol{U}(s')\boldsymbol{\cdot}\left[2\boldsymbol{I} - \boldsymbol{t}(s')\boldsymbol{t}(s')\right]\boldsymbol{\cdot}\mathbf{G}(s,s')\right\}\mathrm{d}s', \tag{4.44a}$$

$$\mathbf{G}(s,s') = \frac{\boldsymbol{I}}{R_0} + \frac{\boldsymbol{R}_0\boldsymbol{R}_0}{R_0^3}, \tag{4.44b}$$

$\boldsymbol{U} = \boldsymbol{U}\boldsymbol{\cdot}(\boldsymbol{tt} + \boldsymbol{i}_2\boldsymbol{i}_2)$ and $\boldsymbol{I} = \boldsymbol{tt} + \boldsymbol{i}_2\boldsymbol{i}_2 + \boldsymbol{i}_3\boldsymbol{i}_3$. The final result in (4.43) forms a slip RFT, accurate to order $1/\ln^2\epsilon$. When $\Lambda = 0$, this result agrees with the no-slip result from Cox (1970). The results are compared with the two other formulations and with numerical computations in § 5.

## 4.2. *Keller–Rubinow–Johnson slender-body theory formulation*

The second expansion we perform is in the form of the Keller–Rubinow–Johnson (KRJ) SBT. The KRJ SBT is the most popular version of SBT used today because of its accuracy. Similarly to the rod case, it can be derived using point forces, and source dipoles and asymptotically enforcing the boundary conditions. This representation was first derived by Keller & Rubinow (1976) and re-derived and extended by Johnson (1980) by considering additional singularity solutions. Götz (2000) later showed how the formulation can be derived using a traditionally structured matched asymptotic formalism on the singularities.

A KRJ SBT with slip can also be derived using stokeslets (point forces) and source dipoles but enforcing the slip boundary conditions (2.12), instead of the classic no-slip conditions. Inspired by the solution for straight rods with a constant force density (see § 3), we anticipate that the dipole strength is related to the force through

$$\boldsymbol{g}(s) = \frac{\chi b^2}{2}\boldsymbol{f}(s). \tag{4.45}$$

If this guess dipole strength can be shown to satisfy the boundary conditions, we know that this must be the solution because solutions to Stokes flows are unique. The flow and strain near the surface of the slender body are therefore given by

$$8\pi \boldsymbol{u}(\boldsymbol{r}) = \int_0^1 \mathrm{d}s' \left[ \left( \frac{\boldsymbol{I}}{R} + \frac{\boldsymbol{R}\boldsymbol{R}}{R^3} \right) \boldsymbol{\cdot} \boldsymbol{f}(s') + \chi b^2 \left( \frac{\boldsymbol{I}}{R^3} - \frac{3\boldsymbol{R}\boldsymbol{R}}{R^5} \right) \boldsymbol{\cdot} \boldsymbol{f}(s') \right], \tag{4.46}$$

$$8\pi \boldsymbol{E}(\boldsymbol{r}) = \int_0^1 \mathrm{d}s' \left( \frac{\boldsymbol{I}}{R^3} - \frac{3\boldsymbol{R}\boldsymbol{R}}{R^5} \right) \boldsymbol{R} \boldsymbol{\cdot} \boldsymbol{f}(s') - 3\chi b^2 \int_0^1 \mathrm{d}s' \left[ \frac{\boldsymbol{R}\boldsymbol{f}(s') + \boldsymbol{f}(s')\boldsymbol{R}}{R^5} + \left( \frac{\boldsymbol{I}}{R^5} - 5\frac{\boldsymbol{R}\boldsymbol{R}}{R^7} \right) \boldsymbol{R} \boldsymbol{\cdot} \boldsymbol{f}(s') \right], \tag{4.47}$$

where again $\boldsymbol{R} = \boldsymbol{r}_c(s) - \boldsymbol{r}_c(s') + r\boldsymbol{e}_r(s)$. Once again, these integrals display two regions of behaviour, an inner region where the body looks locally like a cylinder and an outer region where the body looks like a line. Therefore to construct the KRJ SBT we need to create a composite representation with the flow from each region and enforce the slip boundary conditions to leading order.

### 4.2.1. *Inner region*

In the inner region the body is locally cylindrical and $\boldsymbol{R}_0 = \boldsymbol{r}_c(s) - \boldsymbol{r}_c(s') = O(\epsilon)$. Assuming everything varies slowly on this scale we find

$$\boldsymbol{r}_c\big(s'\big) = \boldsymbol{r}_c(s) + \Delta\, \boldsymbol{t}(s) + O\big(\epsilon^2\big), \tag{4.48}$$

$$\boldsymbol{f}\big(s'\big) = \boldsymbol{f}(s) + O(\epsilon). \tag{4.49}$$

In this region the velocity is

$$8\pi \boldsymbol{u}^I(\boldsymbol{r}_S) = \int_0^1 \mathrm{d}s' \left[ \left( \frac{\boldsymbol{I}}{R_L} + \frac{\boldsymbol{R}_L\boldsymbol{R}_L}{R_L^3} \right) \boldsymbol{\cdot} \boldsymbol{f}(s) + \chi b^2 \left( \frac{\boldsymbol{I}}{R_L^3} - 3\frac{\boldsymbol{R}_L\boldsymbol{R}_L}{R_L^5} \right) \boldsymbol{\cdot} \boldsymbol{f}(s) \right] + O(1), \tag{4.50}$$

where $\boldsymbol{R}_L = \Delta \boldsymbol{t}(s) + r\boldsymbol{e}_r(s)$ and the superscript '$I$' denotes the inner-region representation. Similarly the stress times slip length is

$$\begin{aligned} &16\pi \varLambda (\boldsymbol{I} - \boldsymbol{e}_r\boldsymbol{e}_r) \boldsymbol{\cdot} \boldsymbol{E}^I\Big|_{\boldsymbol{r}=\boldsymbol{r}_S} \boldsymbol{\cdot} \boldsymbol{e}_r \\ &= -6b\varLambda\, \boldsymbol{t}(s) \int_0^1 \mathrm{d}s' \left[ \frac{\varDelta}{R_L^5} \boldsymbol{R}_L \right] \boldsymbol{\cdot} \boldsymbol{f}(s) \\ &\quad - 6\chi b^2 \varLambda \int_0^1 \mathrm{d}s' \left[ \frac{(\boldsymbol{I} - \boldsymbol{e}_r\boldsymbol{e}_r) \boldsymbol{\cdot} \boldsymbol{f}(s) b + \Delta \boldsymbol{t}(s) \boldsymbol{e}_r \boldsymbol{\cdot} \boldsymbol{f}(s)}{R_L^5} \right] \\ &\quad + 30\chi b^3 \varLambda\, \boldsymbol{t}(s) \int_0^1 \mathrm{d}s' \left[ \frac{\varDelta}{R_L^7} \boldsymbol{R}_L \right] \boldsymbol{\cdot} \boldsymbol{f}(s) + O(1). \end{aligned} \tag{4.51}$$

These integrals have been asymptotically evaluated in (3.18) and (4.31). The inner part of the boundary conditions is therefore

$$
\begin{aligned}
8\pi\left[\boldsymbol{u}^I(\boldsymbol{r}_S)-2\varLambda(\boldsymbol{I}-\boldsymbol{e}_r\boldsymbol{e}_r)\boldsymbol{\cdot}\boldsymbol{E}^I\Big|_{\boldsymbol{r}=\boldsymbol{r}_S}\boldsymbol{\cdot}\boldsymbol{e}_r\right]
&=\varPhi\boldsymbol{I}\boldsymbol{\cdot}\boldsymbol{f}(s)+\left(\varPhi-2+\frac{4\varLambda}{b}\right)\boldsymbol{t}(s)\boldsymbol{t}(s)\boldsymbol{\cdot}\boldsymbol{f}(s)\\
&\quad+2\chi\left(1+\frac{4\varLambda}{b}\right)[\boldsymbol{I}-\boldsymbol{t}(s)\boldsymbol{t}(s)]\boldsymbol{\cdot}\boldsymbol{f}(s)+O(\epsilon),
\end{aligned}
\tag{4.52}
$$

where $\varPhi=\ln(4s(1-s)/b^2)$.

In conducting this inner expansion we have assumed that $s$ is not within order $\epsilon$ of the ends of the body. These regions are not significant at leading order, with scaling revealing that end effects contribute at $O(\epsilon^2)$ (Koens & Lauga 2018). A direct result of ignoring these contributions results in the so-called ‘ellipsoidal ends condition’ (Koens & Lauga 2018), which assumes that near the ends $s(1-s)/b^2$ approaches a finite, non-zero value. This condition prevents the logarithm, $\varPhi$, diverging at the edges of the body. The ellipsoidal ends condition is a weak condition for the total force as logarithmic singularities are integrable. We also note that this inner-region result would be the same if the singularities were placed between the ‘ellipsoidal foci’ of the centreline. Again it can be shown that the foci only influence the result at $O(\epsilon^2)$ (Koens & Lauga 2018).

### 4.2.2. *Outer region*

In the outer region the system looks like a line and $\boldsymbol{R}_0=\boldsymbol{r}_c(s)-\boldsymbol{r}_c(s')=O(1)$. The flow and the stress can therefore be written as

$$
\boldsymbol{R}=\boldsymbol{r}_S(s,\theta)-\boldsymbol{r}_c\left(s'\right)=\boldsymbol{R}_0+O(\epsilon),
\tag{4.53}
$$

$$
8\pi\boldsymbol{u}^O(\boldsymbol{r}_S)=\int_0^1 \mathrm{d}s'\left[\left(\frac{\boldsymbol{I}}{R_0}+\frac{\boldsymbol{R}_0\boldsymbol{R}_0}{R_0^3}\right)\boldsymbol{\cdot}\boldsymbol{f}(s')\right]+O(\epsilon),
\tag{4.54}
$$

$$
2\varLambda(\boldsymbol{I}-\boldsymbol{e}_r\boldsymbol{e}_r)\boldsymbol{\cdot}\boldsymbol{E}^O\Big|_{\boldsymbol{r}=\boldsymbol{r}_S}\boldsymbol{\cdot}\boldsymbol{e}_r=0+O(\epsilon),
\tag{4.55}
$$

where the superscript ‘$O$’ indicates the contribution in the outer regions. Hence the outer part of the boundary conditions becomes

$$
\boldsymbol{u}^O(\boldsymbol{r}_S)-2\varLambda(\boldsymbol{I}-\boldsymbol{e}_r\boldsymbol{e}_r)\boldsymbol{\cdot}\boldsymbol{E}^O\Big|_{\boldsymbol{r}=\boldsymbol{r}_S}\boldsymbol{\cdot}\boldsymbol{e}_r=\frac{1}{8\pi}\int_0^1 \mathrm{d}s'\left[\left(\frac{\boldsymbol{I}}{R_0}+\frac{\boldsymbol{R}_0\boldsymbol{R}_0}{R_0^3}\right)\boldsymbol{\cdot}\boldsymbol{f}(s')\right]+O(\epsilon).
\tag{4.56}
$$

### 4.2.3. *Composite solution*

A composite representation for the right-hand side of (2.6) can be constructed from the matched asymptotic forms by adding together in inner- and outer-region solutions and subtracting any common behaviour. Hence the matched asymptotic form of the boundary conditions is

$$
\begin{aligned}
\boldsymbol{U}(s)&=\boldsymbol{u}^O(\boldsymbol{r}_S)-2\varLambda(\boldsymbol{I}-\boldsymbol{e}_r\boldsymbol{e}_r)\boldsymbol{\cdot}\boldsymbol{E}^O\Big|_{\boldsymbol{r}=\boldsymbol{r}_S}\boldsymbol{\cdot}\boldsymbol{e}_r+\boldsymbol{u}^I(\boldsymbol{r}_S)-2\varLambda(\boldsymbol{I}-\boldsymbol{e}_r\boldsymbol{e}_r)\boldsymbol{\cdot}\boldsymbol{E}^I\Big|_{\boldsymbol{r}=\boldsymbol{r}_S}\boldsymbol{\cdot}\boldsymbol{e}_r\\
&\quad-\left(\boldsymbol{u}^C(\boldsymbol{r}_S)-2\varLambda(\boldsymbol{I}-\boldsymbol{e}_r\boldsymbol{e}_r)\boldsymbol{\cdot}\boldsymbol{E}^C\Big|_{\boldsymbol{r}=\boldsymbol{r}_S}\boldsymbol{\cdot}\boldsymbol{e}_r\right)+O(\epsilon),
\end{aligned}
\tag{4.57}
$$

where the superscript ‘C’ denotes the common behaviour.

In our case this common behaviour can be found by expanding the outer solution in terms of the inner-solution variables (or vice versa) and is

$$\boldsymbol{u}^C(\boldsymbol{r}_S) - 2\varLambda(\boldsymbol{I} - \boldsymbol{e}_r\boldsymbol{e}_r)\boldsymbol{\cdot}\boldsymbol{E}^C\Big|_{r=r_S}\boldsymbol{\cdot}\boldsymbol{e}_r = \frac{1}{8\pi}\int_0^1 \mathrm{d}s'\left[\left(\frac{\boldsymbol{I}+\boldsymbol{t}(s)\boldsymbol{t}(s)}{|s-s'|}\right)\boldsymbol{\cdot}\boldsymbol{f}(s)\right] + O(\epsilon). \tag{4.58}$$

Hence the composite asymptotic representation of the boundary condition can be written as

$$\begin{aligned}8\pi\boldsymbol{U}(s) = {} & \int_0^1 \mathrm{d}s'\left[\left(\frac{\boldsymbol{I}}{R_0} + \frac{\boldsymbol{R}_0\boldsymbol{R}_0}{R_0^3}\right)\boldsymbol{\cdot}\boldsymbol{f}(s') - \left(\frac{\boldsymbol{I}+\boldsymbol{t}(s)\boldsymbol{t}(s)}{|s-s'|}\right)\boldsymbol{\cdot}\boldsymbol{f}(s)\right]\\ & + (\varPhi + 2 - 2\chi)\left[\boldsymbol{I} - \boldsymbol{t}(s)\boldsymbol{t}(s)\right]\boldsymbol{\cdot}\boldsymbol{f}(s)\\ & + \left(2\varPhi - 2 + \frac{4\varLambda}{b}\right)\boldsymbol{t}(s)\boldsymbol{t}(s)\boldsymbol{\cdot}\boldsymbol{f}(s) + O(\epsilon),\end{aligned} \tag{4.59}$$

where we remind the reader that $\varPhi = \ln(4s(1-s)/b^2)$. This integral operator has an identical integrand to that of the no-slip case but with a modified local contribution to account for slip. The behaviour of operators with said integrands have therefore been analysed previously by Götz (2000) and have been shown to have solution. Hence, since the above composite expression can satisfy the boundary conditions, uniqueness therefore tells us that (4.59) is the KRJ SBT with the slip correction and can be solved for the unknown force per unit length, $\boldsymbol{f}(s)$, numerically. When the slip length is set to zero, we recover the classical KRJ solution, ensuring consistency with the original no-slip theory. Inspecting the above equation we note that both the left- and right-hand sides of the equations are purely a function of $s$. This confirms that our guess for the dipole strength in (4.45) was correct. If the guess was incorrect the right-hand side of the equation would display dependence on $\theta$ (Götz 2000).

We remind the reader that the error on the KRJ SBT (4.59) is $O(\epsilon)$, though the accuracy of the force density, $\boldsymbol{f}(s)$, found from solving it may be higher. Johnson (1980) demonstrated that, in the no-slip case, the next-order correction to the force density occurs at $O(\epsilon^2\ln(\epsilon))$. Due to the complexity of this process, we will not repeat the calculation here for the slip case, so all we can be sure of is that the force density when slip is present is at least accurate to $O(\epsilon)$.

### 4.3. *Lighthill’s slender-body theory formulation*

In this section, we finally develop a Lighthill SBT representation. This approach has a different structure from the previous methods and reveals information about the inherent size of the inner region in an intuitive manner. Lighthill postulated that the flow around the body could again be represented with stokeslets and source dipoles (satisfying (3.22)). Recalling that $\varDelta = s - s'$ denotes the distance along the centreline, Lighthill argued that there is an intermediate length $\delta$ that satisfies $\epsilon \ll \delta \ll 1$ which defines two regions: the inner region where $|\varDelta| \leqslant \delta$, and the outer region where $|\varDelta| > \delta$. The relative importance of the stokeslets and source dipoles changes in the different regions. In the inner region the flow from the stokeslets is $O(1/\ln\epsilon)$ and from the dipoles is $O(1)$. In the outer region, the flow from the stokeslets is $O(1/\ln\delta)$, while from the dipoles is $O(\epsilon^2/\delta^2)$. This means that while both stokeslets and source dipoles are important to the inner region, only the stokeslets contribute in the outer region. Hence, Lighthill used stokeslets along the entire centreline and added dipoles to the inner region (see sketch in figure 3).

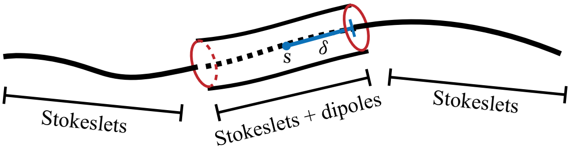

Figure 3. Lighthill's singularity construction for the SBT of flagellar hydrodynamics. To evaluate the flow near the point $s$, the body is separated into inner and outer regions by an intermediate length $\delta$ which satisfies $a \ll \delta \ll L$. The flow is presented as that induced by a line distribution of stokeslets along the whole centreline and dipoles only in the inner region.

Following Lighthill's approach, the slip boundary condition, (2.6), becomes

$$\boldsymbol{U} = \boldsymbol{U}^I + \boldsymbol{U}^O, \tag{4.60a}$$

$$\boldsymbol{U}^I = \left[\boldsymbol{u}_s^I + \boldsymbol{u}_d^I - 2\varLambda(\boldsymbol{I} - \boldsymbol{e}_r\boldsymbol{e}_r)\boldsymbol{\cdot}\left(\boldsymbol{E}_s^I + \boldsymbol{E}_d^I\right)\boldsymbol{\cdot}\boldsymbol{e}_r\right]\Big|_{r=b}, \tag{4.60b}$$

$$\boldsymbol{U}^O = \left[\boldsymbol{u}_s^O - 2\varLambda(\boldsymbol{I} - \boldsymbol{e}_r\boldsymbol{e}_r)\boldsymbol{\cdot}\boldsymbol{E}_s^O\boldsymbol{\cdot}\boldsymbol{e}_r\right]\Big|_{r=b}, \tag{4.60c}$$

where the superscripts '$I$' and '$O$' represent the inner and outer regions, respectively, and the subscripts '$s$' and '$d$' represent the contribution from the stokeslets and source dipoles, respectively. The velocity and strain rates in the above are given by

$$\boldsymbol{u}_s^I = \int_{|\varDelta|\leqslant\delta} \frac{\boldsymbol{f}}{8\pi}\boldsymbol{\cdot}\left(\frac{\boldsymbol{I}}{R} + \frac{\boldsymbol{RR}}{R^3}\right)\mathrm{d}\Delta, \tag{4.61a}$$

$$\boldsymbol{u}_d^I = \int_{|\varDelta|\leqslant\delta} \frac{\boldsymbol{g}}{4\pi}\boldsymbol{\cdot}\left(\frac{\boldsymbol{I}}{R^3} - \frac{3\boldsymbol{RR}}{R^5}\right)\mathrm{d}\Delta, \tag{4.61b}$$

$$\boldsymbol{u}_s^O = \int_{|\varDelta|>\delta} \frac{\boldsymbol{f}}{8\pi}\boldsymbol{\cdot}\left(\frac{\boldsymbol{I}}{R} + \frac{\boldsymbol{RR}}{R^3}\right)\mathrm{d}\Delta, \tag{4.61c}$$

$$\boldsymbol{E}_{s,d}^I = \frac{\boldsymbol{\nabla}\boldsymbol{u}_{s,d}^I + (\boldsymbol{\nabla}\boldsymbol{u}_{s,d}^I)^T}{2}, \quad \boldsymbol{E}_s^O = \frac{\boldsymbol{\nabla}\boldsymbol{u}_s^O + (\boldsymbol{\nabla}\boldsymbol{u}_s^O)^T}{2}. \tag{4.61d}$$

We recall the definition that $\boldsymbol{R} = \boldsymbol{R}_0 + r\boldsymbol{e}_r$ and $\boldsymbol{R}_0 = \boldsymbol{r}_c(s) - \boldsymbol{r}_c(s')$. Since the intermediate length, $\delta$, was artificially introduced, the final form of the expansion should be independent of $\delta$. This can be achieved by asymptotically evaluating the integrals in the inner region. Assuming that the densities of forces and dipoles remain roughly constant over the inner region, we can express their strength by

$$\boldsymbol{f} = f_1\boldsymbol{i}_1 + f_2\boldsymbol{i}_2, \tag{4.62a}$$

$$\boldsymbol{g} = \frac{\chi b^2}{2} f_2\boldsymbol{i}_2, \tag{4.62b}$$

where we used (3.22) for the dipole strength. Substituting the above forms into (4.60a), the inner-flow integrals take the same form as those in (3.18) and (4.31), and so can be approximated as

$$\boldsymbol{u}_s^I = \frac{f_1}{4\pi}\left(2\ln\frac{2\delta}{r} - 1\right)\boldsymbol{i}_1 + \frac{f_2}{4\pi}\left[\ln\frac{2\delta}{r}\boldsymbol{i}_2 + \cos\theta\,\boldsymbol{e}_r\right] + O\left(\frac{r^2}{\delta^2}\right), \tag{4.63a}$$

$$\boldsymbol{u}_d^I = \frac{g}{2\pi r^2}\left[\boldsymbol{i}_2 - 2\cos\theta\,\boldsymbol{e}_r\right] + O\left(\frac{r^2}{\delta^2}\right). \tag{4.63b}$$

The components of the total flow $\boldsymbol{u}_s^I + \boldsymbol{u}_d^I$ are therefore

$$\left[\boldsymbol{u}_s^I + \boldsymbol{u}_d^I\right] \boldsymbol{\cdot} \boldsymbol{i}_1 = \frac{f_1}{4\pi}\left(2\ln\frac{2\delta}{r} - 1\right) + O\left(\frac{r^2}{\delta^2}\right), \tag{4.64a}$$

$$\left[\boldsymbol{u}_s^I + \boldsymbol{u}_d^I\right] \boldsymbol{\cdot} \boldsymbol{e}_r = \frac{f_2\cos\theta}{4\pi}\left(\ln\frac{2\delta}{r} + 1 - \chi\frac{b^2}{r^2}\right) + O\left(\frac{r^2}{\delta^2}\right), \tag{4.64b}$$

$$\left[\boldsymbol{u}_s^I + \boldsymbol{u}_d^I\right] \boldsymbol{\cdot} \boldsymbol{e}_\theta = -\frac{f_2\sin\theta}{4\pi}\left(\ln\frac{2\delta}{r} + \chi\frac{b^2}{r^2}\right) + O\left(\frac{r^2}{\delta^2}\right), \tag{4.64c}$$

where $\boldsymbol{e}_\theta$ is the local cylindrical angular direction.

The slip boundary condition therefore shows that

$$U_1 = \frac{f_1}{4\pi}\left(2\ln\frac{2\delta}{b} - 1 + \frac{2\varLambda}{b}\right) + O\left(\frac{b^2}{\delta^2}\right), \tag{4.65a}$$

$$U_2 = \frac{f_2}{4\pi}\left(\ln\frac{2\delta}{b} + \frac{1}{2} + \frac{\varLambda}{b + 2\varLambda}\right) + O\left(\frac{b^2}{\delta^2}\right), \tag{4.65b}$$

where $\boldsymbol{U}^I = U_1\boldsymbol{i}_1 + U_2\boldsymbol{i}_2$. Though seemingly complex, the above representation can be turned into a more convenient form through the introduction of a new parameter:

$$q(s) = \frac{1}{2}b\exp\left(\frac{1}{2} - \frac{\varLambda}{b}\right). \tag{4.66}$$

This parameter is smaller than $\delta$ and represents a true inner-region length scale. It allows the inner-region velocity to be written as

$$U_1 = \frac{f_1}{2\pi}\ln\frac{\delta}{q}, \tag{4.67a}$$

$$U_2 = \frac{f_2}{4\pi}\left[1 - \frac{2\varLambda^2}{b(b + 2\varLambda)}\right] + \frac{f_2}{4\pi}\ln\frac{\delta}{q}, \tag{4.67b}$$

or

$$\boldsymbol{U}^I(s) = \frac{\boldsymbol{f}_2}{4\pi}\left[1 - \frac{2\varLambda^2}{b(b + 2\varLambda)}\right] + \int_{q(s)<|\varDelta|\leqslant\delta}\frac{\boldsymbol{f}}{8\pi}\boldsymbol{\cdot}\left(\frac{\boldsymbol{I}}{R_0} + \frac{\boldsymbol{R}_0\boldsymbol{R}_0}{R_0^3}\right)\mathrm{d}\Delta, \tag{4.68}$$

as

$$\int_{q(s)<|\varDelta|\leqslant\delta}\frac{\boldsymbol{f}}{8\pi}\boldsymbol{\cdot}\left(\frac{\boldsymbol{I}}{R_0} + \frac{\boldsymbol{R}_0\boldsymbol{R}_0}{R_0^3}\right)\mathrm{d}\Delta = (\boldsymbol{I} + \boldsymbol{tt})\boldsymbol{\cdot}\frac{\boldsymbol{f}}{4\pi}\ln\frac{\delta}{q} + O(\delta). \tag{4.69}$$

The above inner solution can now be connected with the outer-region flow, (4.60*c*) and (4.61*c*). However, it is useful to first simplify this flow before we join the two results. Scaling the respective integrals, $\boldsymbol{u}_s^O$ is $O(1/\ln\delta)$ and $\boldsymbol{E}_s^O$ is $O(\delta^{-1})$; hence, the slip contribution in (4.60*c*) is $\varLambda/\delta$. Since $\varLambda = O(b) = O(\epsilon)$, the contribution from the outer-region stress is $O(\epsilon/\delta) \ll 1$ and so can be neglected from the outer solution. Similarly, the outer-flow integral can be simplified through

$$\boldsymbol{u}_s^O = \int_{|\varDelta|>\delta}\frac{\boldsymbol{f}}{8\pi}\boldsymbol{\cdot}\left(\frac{\boldsymbol{I}}{R} + \frac{\boldsymbol{RR}}{R^3}\right)\mathrm{d}\Delta = \int_{|\varDelta|>\delta}\frac{\boldsymbol{f}}{8\pi}\boldsymbol{\cdot}\left(\frac{\boldsymbol{I}}{R_0} + \frac{\boldsymbol{R}_0\boldsymbol{R}_0}{R_0^3}\right)\mathrm{d}\Delta + O\left(\frac{b}{\delta}\right). \tag{4.70}$$

We note that for bodies with a straight centreline, the error reduces to $O(b^2/\delta^2)$. Adding the simplified terms in the outer and inner flows we find that $\delta$ cancels out and the velocity becomes

$$\boldsymbol{U}(s)=\frac{\boldsymbol{f}_2}{4\pi}\left[1-\frac{2\varLambda^2}{b(b+2\varLambda)}\right]+\frac{1}{8\pi}\int_{|\Delta|>q(s)}\boldsymbol{f}\boldsymbol{\cdot}\left(\frac{\boldsymbol{I}}{R_0}+\frac{\boldsymbol{R}_0\boldsymbol{R}_0}{R_0^3}\right)\mathrm{d}\Delta+O(\delta)+O\left(\frac{\epsilon}{\delta}\right). \tag{4.71}$$

Equation (4.71) is the completed SBT expansion using Lighthill's method. To obtain the tightest error bound, we balance the two remainder terms by setting $\delta=\sqrt{\epsilon}$, which yields a total error $O(\sqrt{\epsilon})$, as in the no-slip case (Childress 1981). This method provides a length scaling for the inner region, $q$. When the slip length is zero, the results reduce to the form in Lighthill (1976) and $q\approx 0.82\epsilon$. However, for finite slip, the length of the local region defined by $q$ decreases exponentially. For instance, slip lengths of $\varLambda/\epsilon=0.5,\ 1$ and 2 produce $q/\epsilon$ of 0.5, 0.3 and 0.1, respectively. This suggests that the effective local region is smaller when slip is present.

We finally note that the end effects in each of the three slip models are expected to be comparable to, or smaller than, those in the classical no-slip case. Slip is a local effect and acts to decrease the force per unit length. Hence, the additional corrections at the ends do not influence the flow in other regions, and the overall end contribution to the net force is likely to be similar or smaller.

## 5. Translation of a prolate spheroid

Equipped with our asymptotic theories, we consider in this section a specific case, the translation of a prolate spheroid (i.e. a shape for which $b(s)=2\epsilon\sqrt{s(1-s)}$), to validate the SBTs and quantify the relationships between them. We use below each theory to solve for the force on the spheroid as it translates parallel and perpendicular to its axis and compare our results with previous numerical studies.

### 5.1. *Implementation of slip resistive-force theory*

First let us solve for the motion of a spheroid using the slip RFT given by (4.43). If we initially take $\boldsymbol{U}=U_1\boldsymbol{i}_1$, the non-local integral becomes

$$\boldsymbol{u}_{NL}^{(1)}=U_1\ln\frac{\delta}{\sqrt{s(1-s)}}\boldsymbol{i}_1, \tag{5.1}$$

which when substituted into (4.43) gives

$$\frac{\boldsymbol{f}^{(1)}}{2\pi}=-U_1\boldsymbol{i}_1,\qquad \frac{\boldsymbol{f}^{(2)}}{2\pi}=\left(\frac{1}{2}-\frac{\varLambda}{b}\right)U_1\boldsymbol{i}_1. \tag{5.2}$$

The force density for a spheroid translating along its axis is therefore predicted to be

$$\frac{f_1(s)}{2\pi U_1}=-\frac{1}{\ln\epsilon}+\frac{1}{\ln^2\epsilon}\left(\frac{1}{2}-\frac{\hat{\varLambda}}{2\sqrt{s(1-s)}}\right)+o\left(\frac{1}{\ln^2\epsilon}\right). \tag{5.3}$$

Similarly for perpendicular translation, where $\boldsymbol{U}=U_2\boldsymbol{i}_2$, the force density becomes

$$\frac{f_2(s)}{4\pi U_2}=-\frac{1}{\ln\epsilon}-\frac{1}{2\ln^2\epsilon}\left(1+\frac{\hat{\varLambda}}{\sqrt{s(1-s)}+\hat{\varLambda}}\right)+o\left(\frac{1}{\ln^2\epsilon}\right). \tag{5.4}$$

Structurally these force densities, (5.3) and (5.4), can be identified as the first few terms in a Taylor series expansion, around $\epsilon = 0$, of

$$\frac{f_1(s)}{2\pi U_1} = \frac{1}{\ln \dfrac{1}{\epsilon} - \dfrac{1}{2} + \dfrac{\varLambda}{b}}, \quad \frac{f_2(s)}{4\pi U_2} = \frac{1}{\ln \dfrac{1}{\epsilon} + \dfrac{1}{2} + \dfrac{\varLambda}{b + 2\varLambda}}. \tag{5.5}$$

The above representation, (5.5), is identical to the force per unit length exerted on the fluid by the rod, obtained in (3.12) and (3.25), when $b \approx \epsilon$. We note that the compact form in (5.5) preserves the same level of accuracy as the asymptotic expressions (5.3) and (5.4).

The compact expressions for the drag per unit length, (5.5), lead naturally to a slip RFT, taking the form

$$\boldsymbol{f} = [\xi_1 \boldsymbol{tt} + \xi_2 (\boldsymbol{I} - \boldsymbol{tt})] \boldsymbol{\cdot} \boldsymbol{U}, \tag{5.6}$$

with slip drag coefficients

$$\xi_1 = \frac{2\pi\mu}{\ln \dfrac{L}{b_0} - \dfrac{1}{2} + \dfrac{\varLambda}{b_0}}, \quad \xi_2 = \frac{4\pi\mu}{\ln \dfrac{L}{b_0} + \dfrac{1}{2} + \dfrac{\varLambda}{b_0 + 2\varLambda}}, \tag{5.7}$$

where $\boldsymbol{t}$ is the unit tangent vector along the filament, and we have restored the units. These drag coefficients reduce to their classical no-slip values when $\varLambda = 0$ (Lighthill 1975) and are accurate to $o(1/\ln^2 \epsilon)$ (as can be concluded from (5.3) and (5.4)).

### 5.2. *Implementation of the KRJ slender-body theory with slip*

Next we solve for the forces on the spheroid using the KRJ slip SBT. The KRJ slip SBT formulation, (4.59), can be solved exactly in this limit. The spheroidal geometry means the logarithmic term becomes $\varPhi = \ln(1/\epsilon^2)$. Assuming that $\varLambda/b$ is constant, (4.59) reduces to

$$\begin{aligned} 8\pi \boldsymbol{U} = {} & [\boldsymbol{I} + \boldsymbol{i}_1\boldsymbol{i}_1] \boldsymbol{\cdot} \int_0^1 \mathrm{d}s' \left[ \frac{\boldsymbol{f}(s') - \boldsymbol{f}(s)}{|s - s'|} \right] \\ & + (\varPhi + 2 - 2\chi)\, [\boldsymbol{I} - \boldsymbol{i}_1\boldsymbol{i}_1] \boldsymbol{\cdot} \boldsymbol{f}(s) + \left( 2\varPhi - 2 + \frac{4\varLambda}{b} \right) \boldsymbol{i}_1\boldsymbol{i}_1 \boldsymbol{\cdot} \boldsymbol{f}(s), \end{aligned} \tag{5.8}$$

where $\boldsymbol{U}$ is the constant centreline velocity. The integral in the above equation has eigenfunctions of Legendre polynomials with the properties

$$\int_0^1 \mathrm{d}s' \left[ \frac{P_n(s') - P_n(s)}{|s - s'|} \right] = -\lambda_n P_n(s), \tag{5.9}$$

where $\lambda_0 = 0$ and $\lambda_n = 2\sum_{i=0}^{n} 1/i$. This suggests that we should let $\boldsymbol{f}(s) = \sum_{n=0}^{\infty} \boldsymbol{f}_n P_n(s)$, to reduce the the equation to

$$8\pi \boldsymbol{U} = (\varPhi + 2 - 2\chi)\, [\boldsymbol{I} - \boldsymbol{i}_1\boldsymbol{i}_1] \boldsymbol{\cdot} \boldsymbol{f}_0 + \left( 2\varPhi - 2 + \frac{4\varLambda}{b} \right) \boldsymbol{i}_1\boldsymbol{i}_1 \boldsymbol{\cdot} \boldsymbol{f}_0, \tag{5.10}$$

$$\boldsymbol{0} = \boldsymbol{f}_n, \tag{5.11}$$

where we have used the orthogonality of Legendre polynomials to separate the modes. The final result in (5.10) is identical to (5.5), thereby demonstrating a direct connection between the two models.

### 5.3. *Implementation of Lighthill's slender-body theory with slip*

Similarly, if we apply Lighthill's formulation to the translating spheroid problem, (4.71) reduces to

$$\boldsymbol{U} = \frac{\boldsymbol{f}_2}{4\pi}\left[1 - \frac{2\varLambda^2}{b(b+2\varLambda)}\right] + \frac{1}{8\pi}\left(\int_{|\varDelta|>q(s)} \frac{\boldsymbol{f}(s')}{|\varDelta|}\mathrm{d}\Delta\right)\boldsymbol{\cdot}(\boldsymbol{I}+\boldsymbol{i}_1\boldsymbol{i}_1), \tag{5.12}$$

which can be simplified if we can evaluate the final integral. This integral can be written as

$$\begin{aligned}\int_{|\varDelta|>q(s)} \frac{\boldsymbol{f}(s')}{|\varDelta|}\,\mathrm{d}\Delta = \int_{|\varDelta|>q(s)} \frac{\boldsymbol{f}(s)}{|\varDelta|}\,\mathrm{d}\Delta + \int_0^1 \frac{\boldsymbol{f}(s') - \boldsymbol{f}(s)}{|\varDelta|}\,\mathrm{d}s' \\ - \int_{|\varDelta|\leqslant q(s)} \frac{\boldsymbol{f}(s') - \boldsymbol{f}(s)}{|\varDelta|}\,\mathrm{d}\Delta.\end{aligned} \tag{5.13}$$

The last integral on the right-hand side can be shown to be order of $\epsilon \ln \epsilon$ using a Taylor series, and so can be ignored. This decomposes the integral into a part with eigenvalues of Legendre polynomials and an additional term. Hence applying (5.9), (5.13) becomes

$$\int_{|\varDelta|>q(s)} \frac{\boldsymbol{f}(s')}{|\varDelta|}\,\mathrm{d}s' = \int_{|\varDelta|>q(s)} \frac{\boldsymbol{f}(s)}{|\varDelta|}\,\mathrm{d}s' - \sum_{i=0}^{n} \lambda_n P_n(s)\boldsymbol{f}_n + O(\epsilon \ln \epsilon). \tag{5.14}$$

The remaining integral on the right-hand side can be evaluated to show

$$\int_{|\varDelta|>q(s)} \frac{1}{|\varDelta|}\,\mathrm{d}\Delta = \ln \frac{s(1-s)}{q^2(s)} = 2\left(\ln\frac{1}{\epsilon} - \frac{1}{2} + \frac{\varLambda}{b}\right). \tag{5.15}$$

The above integral can be inserted into (5.12) and the orthogonality of Legendre polynomials used to reduce the equations to

$$\boldsymbol{U} = \frac{1}{4\pi}\left[1 - \frac{2\varLambda^2}{b(b+2\varLambda)}\right]\boldsymbol{f}_0\boldsymbol{\cdot}(\boldsymbol{I}-\boldsymbol{i}_1\boldsymbol{i}_1) + \frac{1}{4\pi}\left(\ln\frac{1}{\epsilon} - \frac{1}{2} + \frac{\varLambda}{b}\right)\boldsymbol{f}_0\boldsymbol{\cdot}(\boldsymbol{I}+\boldsymbol{i}_1\boldsymbol{i}_1), \tag{5.16}$$

which is again identical to (5.5) and (5.10). This shows that all three asymptotic methods, though derived differently, agree with each other for the translation of a slender prolate spheroid.

### 5.4. *Comparison with computational results*

Our asymptotic results for a prolate spheroid can be compared with existing computational results. Keh & Chang (2008) and Chang & Keh (2011) numerically investigated the drag forces exerted on a prolate spheroid with Navier's slip boundary condition, focusing on translation along and perpendicular to its axis, respectively. The drag forces were calculated numerically using a boundary-collocation method. We now compare their results with our predictions (equation (5.7)).

We plot in figures 4(*a*) and 4(*b*) the drag force for the axial motion of spheroids with aspect ratios $\epsilon = 0.1$ and 0.05, respectively, as a function of varying slip length. The asymptotic results derived in our work are shown in solid lines, while the data from Keh & Chang (2008) appear as diamond markers. The slip SBT results appear to be accurate when the slip length is of the same order as, or smaller than, the thickness of the spheroid; the accuracy then decreases as the slip length grows. This is consistent with our assumption that the slip length is of the same order as the body thickness, i.e. $\varLambda \sim b$. We also note that slip SBT is more accurate for thinner spheroids (results for $\epsilon = 0.05$ are closer to the

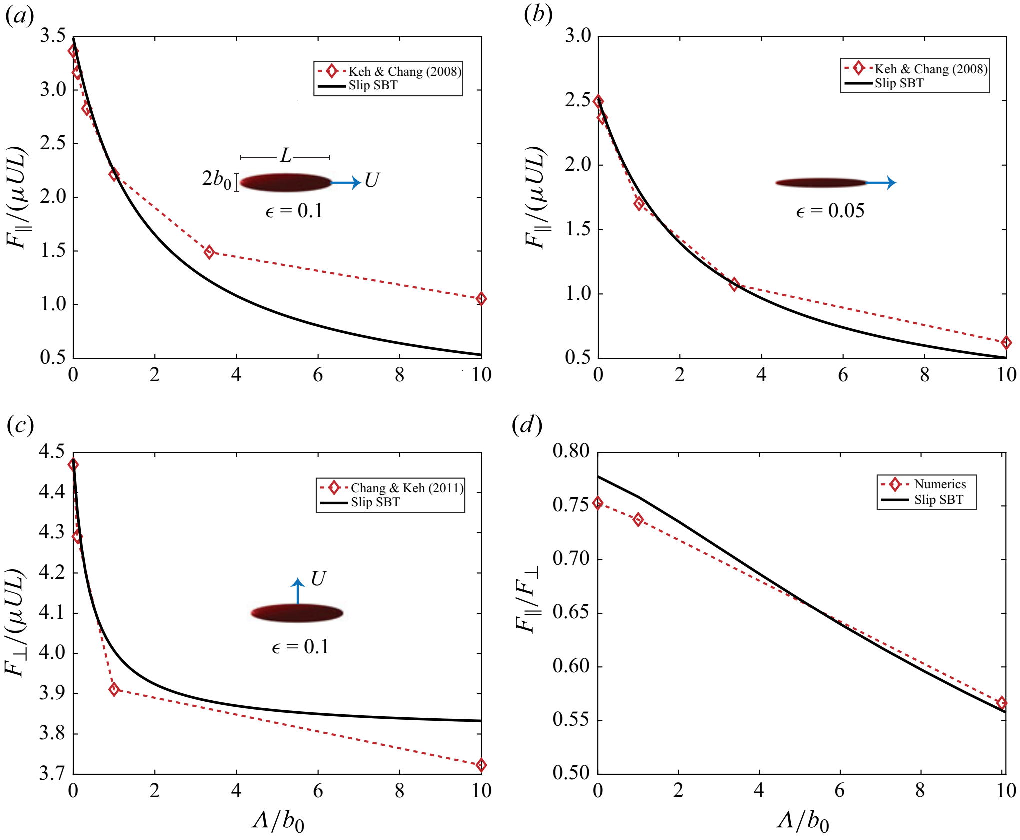

Figure 4. Comparison between our slip SBT, (5.7), and the computational results of Keh & Chang (2008) (parallel motion) and Chang & Keh (2011) (perpendicular). (*a*) Parallel drag on a spheroid with an aspect ratio of $\epsilon = 0.1$. (*b*) Parallel drag on a spheroid with $\epsilon = 0.05$. (*c*) Perpendicular drag on a spheroid with an aspect ratio of $\epsilon = 0.1$. (*d*) Ratio of perpendicular to parallel drag forces with $\epsilon = 0.1$.

computational data), even at relatively large slip lengths. This is also consistent with our expansions that assume $\epsilon \to 0$.

We next show in figure 4(*c*) the drag force from motion perpendicular to the axis of a prolate spheroid with aspect ratio of $\epsilon = 0.1$ (Chang & Keh 2011). Again, slip SBT appears to be accurate for small slip lengths, with the error increasing as the slip length increases beyond the body radius.

We also plot in figure 4(*d*) the ratio between the parallel and perpendicular drag coefficients. We see that it remains very close to the numerical results for all the slip lengths considered. This suggests that the ratio of coefficients remains accurate well beyond the asymptotic limits assumed in the derivation.

## 6. Slip-enhanced propulsion

The newly derived slip resistive force coefficients in (5.7) provide a fast and efficient way to explore the influence of slip on the dynamics of elongated bodies. Here we consider examples in the realm of microswimmer propulsion. To illustrate the leading-order effects of slip, we consider two specific situations of relevance to biological physics: a rotating helical filament (situation applicable to bacterial locomotion) in § 6.1 and a filament with arbitrary planar undulations (case relevant to spermatozoa locomotion and to propulsion generated by artificial active filaments) in § 6.2. We first show that both the models show a similar dependence on the resistance coefficients generally, before discussing the implication for locomotion.

### 6.1. *Propulsion generated by a rotating helical filament*

Helical propulsion is a common locomotion strategy adopted by many flagellated bacteria, such as *E. coli*, and has inspired the design of artificial microswimmers at small scales (Lauga 2016). Here, we consider a force-free finite-torque rotating rigid helix to illustrate the influence of slip on propulsion. This model applies to several magnetically driven helical artificial microswimmers (Zhou *et al.* 2021). We consider a rigid helical filament characterised by the following geometric parameters: helical radius, $R_h$; wavenumber, $\kappa$; helix angle, $\varphi$; total contour length, $L$. We establish a laboratory Cartesian reference frame $[\boldsymbol{j}_x, \boldsymbol{j}_y, \boldsymbol{j}_z]$, in which the centreline of the helix is described by

$$\boldsymbol{r}_c = [R_h \cos(\kappa\alpha s),\ R_h \sin(\kappa\alpha s),\ \alpha s], \tag{6.1}$$

with the tangent vector to this centreline given by

$$\boldsymbol{t} = \frac{\partial \boldsymbol{r}_c}{\partial s} = [-R_h\kappa\alpha \sin(\kappa\alpha s),\ R_h\kappa\alpha \cos(\kappa\alpha s),\ \alpha], \tag{6.2}$$

where $s$ is the arclength coordinate along the centreline, and $\alpha = \cos\varphi$.

The propulsive force along the helix axis due to rotation can be determined using the resistive force formalism in (5.6). Assuming the helix rotates about the $z$ axis with a prescribed angular velocity $\varOmega$, the local velocity at position $s$ is given by

$$\boldsymbol{U} = \varOmega \boldsymbol{j}_z \times \boldsymbol{r}_c = [-\varOmega R_h \sin(\kappa\alpha s),\ \varOmega R_h \cos(\kappa\alpha s),\ 0], \tag{6.3}$$

and the $z$ component of the force per unit length becomes

$$f_{prop} = (\xi_2 - \xi_1)\varOmega R_h^2 \kappa\alpha^2, \tag{6.4}$$

where $\xi_1$ and $\xi_2$ are the tangential and normal drag coefficients, respectively. Integrating along the filament gives a total propulsive force of

$$F_{prop} = (\xi_2 - \xi_1)\varOmega R_h^2 \kappa\alpha^2 L. \tag{6.5}$$

For swimming, we consider the idealised case of a headless rotating helix. In this set-up, the system is force-free but not torque-free, since an external torque is required to sustain the rotation. The propulsive force generated by rotation is therefore balanced by the translational drag. Assuming translation of the helix along its $z$ axis only, $\boldsymbol{U} = [0, 0, U_z]$, the force per unit length in the $z$ direction becomes

$$f_{drag} = [\alpha^2(\xi_2 - \xi_1) - \xi_2]U_z, \tag{6.6}$$

and the total drag force has value

$$F_{drag} = [\alpha^2(\xi_2 - \xi_1) - \xi_2]LU_z. \tag{6.7}$$

The unknown velocity $U_z$ can then be determined by enforcing the force-free condition, $F_{prop} + F_{drag} = 0$, which yields

$$\frac{U_z}{\varOmega R_h} = \frac{\zeta}{1 - \alpha^2\zeta}\alpha^2 R_h \kappa, \tag{6.8}$$

where $\zeta$ is one minus the ratio of the drag coefficients, defined as

$$\zeta = \frac{\xi_2 - \xi_1}{\xi_2}. \tag{6.9}$$

We note that (6.8) has the same form as in the classical no-slip case, but here the drag coefficients are modified by the slip length, as given in (5.7). Importantly, as the slip length grows, $\zeta$ increases, leading to a higher swimming velocity of the helix.

### 6.2. *Waving filament propulsion*

Undulatory flagellar propulsion is a fundamental mechanism observed in spermatozoa and has also inspired the design of artificial microswimmers (Lauga & Powers 2009). Motivated by these systems, we consider the classical waving-sheet model of Lighthill (1975), where the filament has an arbitrary waveform and each material point is assumed to move only in the vertical direction. In a two-dimensional fixed (laboratory) reference frame, $[\boldsymbol{j}_x, \boldsymbol{j}_y]$, with the wave propagating in the $x$ direction at speed $V$, the velocity of a material point on the filament can be expressed as

$$\boldsymbol{U} = -\frac{V}{\vartheta}\boldsymbol{t} + (V - U_x)\boldsymbol{j}_x, \tag{6.10}$$

where $\vartheta$ is the ratio of the axial wavelength to the contour wavelength, $U_x$ is the translational swimming speed and $\boldsymbol{t}$ is the local tangential direction along the sheet (which is time-independent in the wave frame).

According to RFT, the local hydrodynamic force per unit length in the $x$ direction is

$$f = \left[\xi_1 \frac{x_s}{\vartheta} - \xi_1 x_s^2 - \xi_2\left(1 - x_s^2\right)\right] V + \left[\xi_1 x_s^2 + \xi_2\left(1 - x_s^2\right)\right] U_x, \tag{6.11}$$

where $x_s = \boldsymbol{t} \boldsymbol{\cdot} \boldsymbol{j}_x$, and $\xi_1$, $\xi_2$ are again the tangential and normal drag coefficients. Integrating over the total arclength $L$ and using

$$\int_0^L x_s \,\mathrm{d}s = L\vartheta, \qquad \int_0^L x_s^2 \,\mathrm{d}s = L\beta, \tag{6.12}$$

the total force on the filament becomes

$$F = -(\xi_2 - \xi_1)(1 - \beta)LV - [\beta(\xi_2 - \xi_1) - \xi_2]U_x L, \tag{6.13}$$

where $\beta$ is a constant less than 1. Hence, when the filament is force-free, the translational velocity becomes

$$\frac{U_x}{V} = \frac{\zeta}{1 - \beta\zeta}(1 - \beta). \tag{6.14}$$

Here also, the final result is formally identical to that found by Lighthill (1975), to within the slip-adjusted values of the drag coefficients. Again, we find that as $\zeta$ increases, the swimming speed of the waving filament also increases.

### 6.3. *The effect of slip on locomotion*

The results in (6.8) and (6.14) both show that the swimming velocity of both a helix and a waving filament increases as the dimensionless coefficient $\zeta = (\xi_2 - \xi_1)/\xi_2$ increases. The effect of slip on the propulsion for these two types of swimmers can therefore be understood using the slip drag coefficients, (5.5), and investigating how $\zeta$ changes with the slip length. In figure 4(*d*), we saw that the ratio of parallel to perpendicular drag coefficients decreases monotonically as the slip length, $\Lambda$, increases. Hence, $\zeta$ increases

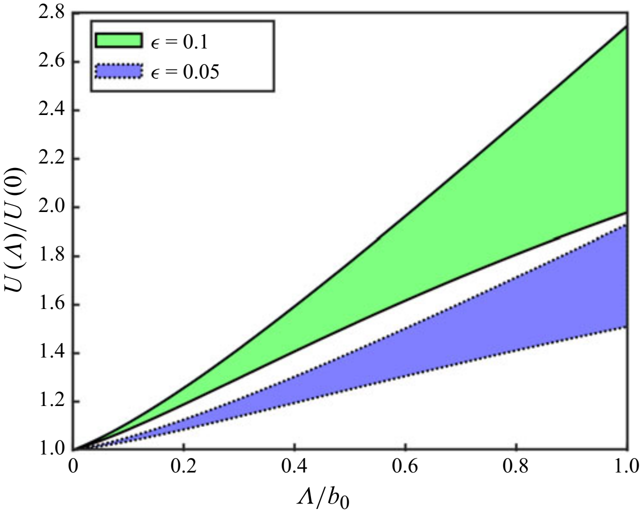

Figure 5. The range of velocities of the helical and waving filament as the slip length increases. All velocities are scaled by their non-slip equivalent. The range represents the [0, 1] spread of $\alpha$ (helix) and $\beta$ (filament). The green region with the solid outline corresponds to velocities when $\epsilon = 0.1$ and the blue region with the dotted outline corresponds to velocities when $\epsilon = 0.05$.

as $\Lambda$ increases, and therefore the swimming speed is enhanced for both swimmers with increasing slip. This is expected as, in our model, increasing $\Lambda$ decreases the parallel drag $\xi_1$ towards 0, while $\xi_2$ decreases to an asymptotic value.

We consider the swimming speeds obtained in (6.8) and (6.14) as functions of the slip length $\Lambda$ and examine the normalised speed $U(\Lambda)/U(0)$. Since $\alpha^2$ and $\beta$ lie in (0, 1), this speed ratio can be bounded by

$$\frac{\zeta(\Lambda)}{\zeta(0)} \leqslant \frac{U(\Lambda)}{U(0)} \leqslant \frac{\zeta(\Lambda)}{1-\zeta(\Lambda)} \frac{1-\zeta(0)}{\zeta(0)}. \tag{6.15}$$

We plot in figure 5 the bounded regions for the swimming speed as a function of slip length. We find that even for relatively small slip lengths there is a measurable increase in the swimming speed. This supports the hypothesis that slip could explain some of the enhanced swimming seen in polymer solutions (Gagnon *et al.* 2013; Patteson *et al.* 2015; Zöttl & Yeomans 2019).

## 7. Discussion and conclusion

Slip effects on solid boundaries are prevalent in various complex environments and thus theoretical frameworks are needed to explore and understand their impact. In this paper we extended the classical theories for the mobility of slender bodies to include surface slip. The slip boundary is modelled using Navier's slip condition, in which the tangential slip velocity is linearly proportional to the shear rate along the surface, captured through a single parameter: the slip length $\Lambda$. We performed three classical expansions for the force per unit length on a slender body, each of which expand the flow in terms of the aspect ratio of the body, $\epsilon = b/L$, before validating them against existing computational results. The main theoretical frameworks we have developed are a slip RFT (5.6), (5.7); a slip KRJ SBT (4.59); and a slip Lighthill SBT (4.71). Together they provide complementary trade-offs between accuracy and convenience, and all reduce to the no-slip limit as $\Lambda \to 0$.

These general formulations are grounded in a preliminary analysis of a straight rod with slip, which provides physical intuition and the local drag laws used later. The drag coefficients tangential and perpendicular to the axis of the rod were asymptotically found using a hydrodynamic singularity approach inspired by the classical studies of Lighthill (1975) and Hancock (1953). The slip boundary condition requires the ratio of the source dipole strength to the stokelet strength to be $b^3/4(b+2\varLambda)$. The corresponding ratio in the non-slip case is $b^2/4$ (Lighthill 1975). The tangential and perpendicular drag coefficients naturally lead to the slip RFT and the ratio of source dipoles and stokeslets supports the derivation of the SBT models following Keller & Rubinow (1976), Johnson (1980) and Lighthill (1976).

Building on the straight-rod intuition, we then developed three types of SBT in detail. First we generated a logarithmic expansion, similar to that in Cox (1970). Next we developed a KRJ formulation through a matched asymptotic expansion applied to a distribution of stokeslets and source dipoles. The resultant equations, (4.59), are accurate to $O(\epsilon)$. Finally Lighthill's formulation, (4.71), introduces an intermediate scale to construct an asymptotic model accurate to $O(\epsilon^{1/2})$. In each model, slip significantly changes the local drag when $\epsilon$ is small but finite (e.g. $\varLambda/\ln(1/\epsilon)=O(1)$). The size of the local region decreases as the slip length increases and the denominator of the local drag for motion parallel to the filament axis gains a $+\varLambda/b$ term and the perpendicular drag gains a $+\varLambda/(b+2\varLambda)$ term, (5.7). Hence, as the slip length gets large, the perpendicular drag asymptotes to a reduced non-zero value of $4\pi\mu/[\ln(1/\epsilon)+1]$ as $\varLambda$ increases while the parallel drag decreases to 0. Consequently, in the case of perfect slip, the parallel drag may become negligible. Though large slip is formally outside the limits of our asymptotic expansions, the ratio of the parallel and perpendicular drag forces appears to remain accurate for $\varLambda/b$ up to 10 (figure 4*d*) and displays a systematic decrease as the slip length increases.

The solution of a translating prolate spheroid was then considered using each model. This demonstrated how to implement each formulation and showed that these theories are consistent with one another and with the no-slip results in the $\varLambda\rightarrow 0$ limit. These representations were also seen to capture well the numerical results for a translating spheroid with slip when the slip length is of the order of the aspect ratio, $\epsilon$. The error, however, increased as the slip length, $\varLambda$, got larger (figure 3).

Finally we applied the slip model to the swimming of a rotating helix and an arbitrary undulating filament. In both cases the swimming speed is found to increase as the ratio of the parallel to perpendicular drag coefficients decreases, through a common dependence. Since increasing the slip length, $\varLambda$, monotonically decreases this ratio, it is confirmed that slip and slip-like effects will enhance the swimming speed of microorganisms and micromachines.

The models presented here could be extended in several ways. We have assumed that the slip length is of the order of the body thickness. However, this length can become larger than the thickness (Montenegro-Johnson *et al.* 2012). It would be valuable to explore these scenarios, potentially resolving the slip layer by incorporating a viscosity gradient. Additionally, while we focused on the apparent slip effect seen in some non-Newtonian fluids, we have neglected any non-Newtonian rheology. Future studies could investigate the effect of slip in weakly non-Newtonian fluids to shed light on how non-Newtonian rheology affects the mobility of a general slender-shaped swimmer. Another possible extension would be to incorporate local rotation of the slender body, which may influence propulsion in systems with torsional motion.

**Funding.** This work was supported by the National Natural Science Foundation of China (NSFC) through the Excellence Research Group Program for Multiscale Problems in Nonlinear Mechanics (grant no. 12588201) and the General Program (grant no. 12372258, to Y.M.).

**Declaration of interests.** The authors report no conflict of interest.

## REFERENCES

BATCHELOR, G.K. 1970 Slender-body theory for particles of arbitrary cross-section in Stokes flow. *J. Fluid Mech.* **44** (3), 419–440.

BORKER, N.S. & KOCH, D.L. 2019 Slender body theory for particles with non-circular cross-sections with application to particle dynamics in shear flows. *J. Fluid Mech.* **877**, 1098–1133.

CHANG, Y.C. & KEH, H.J. 2011 Theoretical study of the creeping motion of axially and fore-and-aft symmetric slip particles in an arbitrary direction. *Eur. J. Mech.-B/Fluids* **30** (2), 236–244.

CHILDRESS, S. 1981 *Mechanics of Swimming and Flying*. Cambridge University Press.

CHOI, C.-H., WESTIN, K.J.A. & BREUER, K.S. 2003 Apparent slip flows in hydrophilic and hydrophobic microchannels. *Phys. Fluids* **15** (10), 2897–2902.

CHWANG, A.T. & WU, T.Y.-T. 1975 Hydromechanics of low-Reynolds-number flow. Part 2. Singularity method for Stokes flows. *J. Fluid Mech.* **67** (4), 787–815.

COHEN, Y. & METZNER, A.B. 1985 Apparent slip flow of polymer solutions. *J. Rheol.* **29** (1), 67–102.

COX, R.G. 1970 The motion of long slender bodies in a viscous fluid Part 1. General theory. *J. Fluid Mech.* **44** (4), 791–810.

DEMIR, E., LORDI, N., DING, Y. & PAK, O.S. 2020 Nonlocal shear-thinning effects substantially enhance helical propulsion. *Phys. Rev. Fluids* **5** (11), 111301.

GAGNON, D.A., SHEN, X.N. & ARRATIA, P.E. 2013 Undulatory swimming in fluids with polymer networks. *Europhys. Lett.* **104** (1), 14004.

GILLIES, E.A., CANNON, R.M., GREEN, R.B. & PACEY, A.A. 2009 Hydrodynamic propulsion of human sperm. *J. Fluid Mech.* **625**, 445–474.

VAN GOGH, B., DEMIR, E., PALANIAPPAN, D. & PAK, O.S. 2022 The effect of particle geometry on squirming through a shear-thinning fluid. *J. Fluid Mech.* **938**, A3.

GÓMEZ, S., GODÍNEZ, F.A., LAUGA, E. & ZENIT, R. 2017 Helical propulsion in shear-thinning fluids. *J. Fluid Mech.* **812**, R3.

GÖTZ, T. 2000 Interactions of fibers and flow: asymptotics, theory and numerics. PhD thesis, University of Kaiserslautern, Kaiserslautern, Germany.

GUGLIELMINI, L., KUSHWAHA, A., SHAQFEH, E.S.G. & STONE, H.A. 2012 Buckling transitions of an elastic filament in a viscous stagnation point flow. *Phys. Fluids* **24** (12), 123601.

HANCOCK, G.J. 1953 The self-propulsion of microscopic organisms through liquids. *Proc. R. Soc. Lond. Ser. A Math. Phys. Sci.* **217**(1128), 96–121.

HEWITT, D.R. & BALMFORTH, N.J. 2018 Viscoplastic slender-body theory. *J. Fluid Mech.* **856**, 870–897.

JAWED, M K., KHOURI, N K., DA, F., GRINSPUN, E. & REIS, P M. 2015 Propulsion and instability of a flexible helical rod rotating in a viscous fluid. *Phys. Rev. Lett.* **115** (16), 168101.

JOHNSON, R.E. 1980 An improved slender-body theory for Stokes flow. *J. Fluid Mech.* **99** (2), 411–431.

KAMAL, C., GRAVELLE, S. & BOTTO, L. 2020 Hydrodynamic slip can align thin nanoplatelets in shear flow. *Nat. Commun.* **11** (1), 2425.

KEH, H.J. & CHANG, Y.C. 2008 Slow motion of a slip spheroid along its axis of revolution. *Intl J. Multiphase Flow* **34** (8), 713–722.

KELLER, J.B. & RUBINOW, S.I. 1976 Slender-body theory for slow viscous flow. *J. Fluid Mech.* **75** (4), 705–714.

KOENS, L. 2022 Tubular-body theory for viscous flows. *Phys. Rev. Fluids* **7**, 034101.

KOENS, L. & LAUGA, E. 2016 Slender-ribbon theory. *Phys. Fluids* **28** (1), 013101.

KOENS, L. & LAUGA, E. 2018 The boundary integral formulation of Stokes flows includes slender-body theory. *J. Fluid Mech.* **850**, R1.

KOENS, L. & MONTENEGRO-JOHNSON, T.D. 2021 Local drag of a slender rod parallel to a plane wall in a viscous fluid. *Phys. Rev. Fluids* **6**, 064101.

KOENS, L. & WALKER, B.J. 2024 Viscous tubular-body theory for plane interfaces. *J. Fluid Mech.* **979**, A38.arXiv: 2303.17275.

LAUGA, E. 2016 Bacterial hydrodynamics. *Annu. Rev. Fluid Mech.* **48**, 105–130.

LAUGA, E. 2020 *The Fluid Dynamics of Cell Motility*. Cambridge University Press.

LAUGA, E. & POWERS, T.R. 2009 The hydrodynamics of swimming microorganisms. *Rep. Prog. Phys.* **72** (9), 096601.

Li, G., Lauga, E. & Ardekani, A.M. 2021 Microswimming in viscoelastic fluids. *J. Non-Newtonian Fluid Mech.* **297**, 104655.

Lighthill, J. 1976 Flagellar hydrodynamics. *SIAM Rev.* **18** (2), 161–230.

Lighthill, S.J. 1975 *Mathematical Biofluiddynamics*. SIAM.

Man, Y., Koens, L. & Lauga, E. 2016 Hydrodynamic interactions between nearby slender filaments. *Europhys. Lett.* **116** (2), 24002.

Man, Y. & Lauga, E. 2015 Phase-separation models for swimming enhancement in complex fluids. *Phys. Rev. E* **92** (2), 023004.

Maxian, O. & Donev, A. 2022 Slender body theories for rotating filaments. *J. Fluid Mech.* **952**, A5.

Mhetar, V. & Archer, L.A. 1998 Slip in entangled polymer solutions. *Macromolecules* **31** (19), 6639–6649.

Montenegro-Johnson, T.D., Smith, A.A., Smith, D.J., Loghin, D. & Blake, J.R. 2012 Modelling the fluid mechanics of cilia and flagella in reproduction and development. *Eur. Phys. J. E* **35**, 1–17.

Mori, Y. & Ohm, L. 2021 Accuracy of slender body theory in approximating force exerted by thin fiber on viscous fluid. *Stud. Appl. Math.* **147** (1), 127–179.

Nassios, J. & Sader, J.E. 2012 Asymptotic analysis of the Boltzmann–BGK equation for oscillatory flows. *J. Fluid Mech.* **708**, 197–249.

Navier, C.L.M.H. 1823 Mémoire sur les lois du mouvement des fluides. *Mémoires De l'Académie Royale Des Sciences De l'Institut De France* **6**(,1823), 389–440.

Ohm, L. 2024 Well-posedness of a viscoelastic resistive force theory and applications to swimming. *J. Nonlinear Sci.* **34** (5), 82.

Patlazhan, S. & Vagner, S. 2017 Apparent slip of shear thinning fluid in a microchannel with a superhydrophobic wall. *Phys. Rev. E* **96** (1), 013104.

Patteson, A.E., Gopinath, A., Goulian, M. & Arratia, P.E. 2015 Running and tumbling with E. coli in polymeric solutions. *Sci. Rep.-UK* **5** (1), 15761.

Qu, Z. & Breuer, K.S. 2020 Effects of shear-thinning viscosity and viscoelastic stresses on flagellated bacteria motility. *Phys. Rev. Fluids* **5** (7), 073103.

Riley, E.E., Das, D. & Lauga, E. 2018 Swimming of peritrichous bacteria is enabled by an elastohydrodynamic instability. *Sci. Rep.-UK* **8** (1), 10728.

Riley, E.E. & Lauga, E. 2017 Empirical resistive-force theory for slender biological filaments in shear-thinning fluids. *Phys. Rev. E* **95** (6), 062416.

Rodenborn, B., Chen, C.-H., Swinney, H.L., Liu, B. & Zhang, H.P. 2013 Propulsion of microorganisms by a helical flagellum. *Proc. Natl Acad. Sci.* **110** (5), E338–E347.

Roper, M., Dreyfus, R., Baudry, J., Fermigier, M., Bibette, J. & Stone, H.A. 2006 On the dynamics of magnetically driven elastic filaments. *J. Fluid Mech.* **554**, 167–190.

Roselli, R.J. & Diller, K.R. 2011 Rheology of biological fluids. In *Biotransport: Principles and Applications*, pp. 107–168. Springer.

Shelley, M.J. 2016 The dynamics of microtubule/motor-protein assemblies in biology and physics. *Annu. Rev. Fluid Mech.* **48**, 487–506.

Smith, D.J., Gaffney, E.A., Blake, J.R. & Kirkman-Brown, J.C. 2009 Human sperm accumulation near surfaces: a simulation study. *J. Fluid Mech.* **621**, 289–320.

Spagnolie, S.E. & Underhill, P.T. 2023 Swimming in complex fluids. *Annu. Rev. Condens. Matt. Phys.* **14**, 381–415.

Tocci, G., Joly, L. & Michaelides, A. 2014 Friction of water on graphene and hexagonal boron nitride from ab initio methods: very different slippage despite very similar interface structures. *Nano Lett.* **14** (12), 6872–6877.

Walker, B.J., Ishimoto, K. & Gaffney, E.A. 2023 Hydrodynamic slender-body theory for local rotation at zero Reynolds number. *Phys. Rev. Fluids* **8** (3), 034101.

Walther, J.H., Werder, T., Jaffe, R.L. & Koumoutsakos, P. 2004 Hydrodynamic properties of carbon nanotubes. *Phys. Rev. E* **69**, 062201.

Zhou, H., Mayorga-Martinez, C.C., Pané, S., Zhang, L. & Pumera, M. 2021 Magnetically driven micro and nanorobots. *Chem. Rev.* **121** (8), 4999–5041.

Zhu, G., van Gogh, B., Zhu, L., Pak, O.S. & Man, Y. 2024 Self-diffusiophoretic propulsion of a spheroidal particle in a shear-thinning fluid. *J. Fluid Mech.* **986**, A39.

Zöttl, A. & Yeomans, J.M. 2019 Enhanced bacterial swimming speeds in macromolecular polymer solutions. *Nat. Phys.* **15** (6), 554–558.